



Global seamless and high-resolution temperature dataset (GSHTD), 2001–2020



Rui Yao^{a,b,d}, Lunche Wang^{a,b,c,*}, Xin Huang^{d,e}, Qian Cao^{a,c}, Jing Wei^h, Panxing He^{i,j}, Shaoqiang Wang^{a,c}, Lizhe Wang^{f,g,c}

^a Hubei Key Laboratory of Regional Ecology and Environmental Change, School of Geography and Information Engineering, China University of Geosciences, Wuhan, 430074, China

^b Hubei Luojia Laboratory, Wuhan, 430079, China

^c National Engineering Research Center for Geographic Information System, China University of Geosciences, Wuhan, 430074, China

^d School of Remote Sensing and Information Engineering, Wuhan University, Wuhan, 430079, China

^e State Key Laboratory of Information Engineering in Surveying, Mapping and Remote Sensing, Wuhan University, Wuhan, 430079, China

^f School of Computer Science, China University of Geosciences, Wuhan, 430074, China

^g Hubei Key Laboratory of Intelligent Geo-Information Processing, China University of Geosciences, Wuhan, 430074, China

^h Department of Atmospheric and Oceanic Science, Earth System Science Interdisciplinary Center, University of Maryland, College Park, USA

ⁱ Ministry of Education Key Laboratory for Western Arid Region Grassland Resources and Ecology, College of Grassland and Environment Sciences, Xinjiang Agricultural University, Urumqi, 830000, China

^j Ministry of Education Key Laboratory for Biodiversity Science and Ecological Engineering, Institute of Biodiversity Science, Fudan University, Shanghai, 200438, China

ARTICLE INFO

Edited by Jing M. Chen

Keywords:

Near-surface air temperature
Land surface temperature
Gapfilling
Reconstruction
Remote sensing
Machine learning

ABSTRACT

Land surface temperature (Ts) and near-surface air temperature (Ta) are key parameters in multiple research fields. In this study, a global seamless (without missing values) and high-resolution (30 arcsecond spatial resolution) temperature (for both Ts and Ta) dataset (GSHTD) from 2001 to 2020 was developed. First, a method called the estimation of the temperature difference (ETD) was proposed to reconstruct both clear- and cloudy-sky Ts. A global seamless 8-day and monthly average all- and clear-sky Ts data were then created using the MODIS Ts data and the ETD method. The seamless monthly average of the mean, maximum and minimum Ta data were further developed using the seamless Ts data, in situ Ta data and Cubist machine learning algorithm. GSHTD has four main advantages. First, GSHTD includes seven types of temperature data: clear-sky daytime and nighttime Ts, all-sky daytime and nighttime Ts, and mean, maximum and minimum Ta. Second, it has global coverage and high spatial resolution. Third, using the ETD method proposed in this study, GSHTD has no missing values. Fourth, the accuracy of GSHTD is high; the average mean absolute errors (MAEs) of ETD in reconstructing the 25 × 25 and 150 × 150 pixel clear-sky daytime (nighttime) Ts data were 0.724 (0.552) and 1.024 (0.895) °C, respectively. The MAEs of ETD were on average 23.2% and 23.7% lower than those of Remotely Sensed Daily Land Surface Temperature reconstruction (RSDLST) and interpolation of the mean anomalies (IMAs). The MAEs of the estimated monthly average of the mean, maximum and minimum Ta data were 0.797, 0.994 and 1.056 °C, respectively. The developed GSHTD is freely available at Middle Yangtze River Geoscience Data Center (<https://cjgeodata.cug.edu.cn/#/pageDetail?id=97>), which will be useful in many studies related to climate change, environmental science and ecology, and epidemiology and human health.

1. Introduction

The land surface temperature (Ts) and near-surface air temperature (Ta) represent the temperatures of the Earth's surface and the air at a height of 2 m, respectively. They are critical variables in multiple research fields (Chadburn et al., 2017; Weiss et al., 2014b; Yao et al.,

2019; Zeng et al., 2017; Zhang et al., 2017; Liu et al., 2021). Ts and Ta are generally monitored by remote sensors onboard satellites (or aircraft platforms) and meteorological stations on the ground, respectively. However, the Ts and Ta data obtained have some limitations. Firstly, satellite-derived Ts data contain many invalid values, mainly resulting from cloud contaminations (Duan et al., 2017; Li et al., 2018a; Yao et al.,

* Corresponding author at: School of Geography and Information Engineering, China University of Geosciences, Wuhan 430074, China.
E-mail address: wang@cug.edu.cn (L. Wang).

2020b). For instance, Li et al. (2018a) showed that the proportion of invalid values was higher than 70% in the Moderate Resolution Imaging Spectroradiometer (MODIS) MYD11A1 Ts product in the conterminous United States. These missing values will undoubtably affect the use of Ts data (Hu and Brunsell, 2013; Yang et al., 2020; Zhang et al., 2016). For example, Zhang et al. (2016) mapped daily Ta in the Tibetan Plateau using MODIS Ts and in situ Ta data. The final developed Ta map was missing 14% of the values due to the incomplete MODIS Ts data. Furthermore, the in situ Ta data also have some limitations. (1) Most stations are located in urban and suburban areas. These stations are affected by the urban heat island (UHI) effect, which may lead to the overestimation of global warming (Ren and Zhou, 2014; Sun et al., 2016; Wang et al., 2015). (2) There are few weather stations in mountainous and polar regions. For example, in the western Tibetan Plateau of China, there are no weather stations in some of the $2.5^\circ \times 2.5^\circ$ grid areas (Wang et al., 2015). This makes it difficult to fully reveal climate change in these areas. Therefore, spatially continuous Ts and Ta data are urgently required.

Various methods have been developed to reconstruct the missing values in the MODIS Ts data. These gapfilling methods can be classified into the reconstruction of clear-sky Ts (Crosson et al., 2012; Gerber et al., 2018; Li et al., 2018a; Militino et al., 2019b; Sun et al., 2017; Weiss et al., 2014a) and cloudy-sky Ts (Duan et al., 2017; Liu et al., 2019; Long et al., 2020; Wang et al., 2019; Zeng et al., 2018; Zhao and Duan, 2020). The first and second types of methods reconstruct clear-sky (unreal) Ts and cloudy-sky (real) Ts, respectively, under cloudy conditions. The first type of method generally can be classified into four subclasses: (1) the use of neighboring pixels to reconstruct the missing Ts (i.e., spatial reconstruction) (Neteler, 2010; Ke et al., 2013); (2) the use of images at neighboring date to reconstruct the missing Ts (i.e., temporal reconstruction) (Xu and Shen, 2013; Li et al., 2020); (3) the use of other similar Ts products to fill the gaps (Coops et al., 2007; Crosson et al., 2012); (4) the use of more than one type of information to fill the gaps (i.e., hybrid method) (Weiss et al., 2014a; Collins et al., 2017; Gerber et al., 2018; Pham et al., 2019; Militino et al., 2019a; Militino et al., 2019b; Sun et al., 2017; Li et al., 2018a; Yao et al., 2021b). Early studies generally used only one type of information to fill the gaps (Neteler, 2010; Ke et al., 2013; Xu and Shen, 2013; Coops et al., 2007; Crosson et al., 2012). Recently, the hybrid methods that simultaneously using spatial and temporal information were widely developed and achieved better accuracy (Gerber et al., 2018; Militino et al., 2019a; Li et al., 2018a). The cloudy-sky Ts can be reconstructed using: (1) passive microwave subsurface temperature data (Duan et al., 2017; Shwetha and Kumar, 2016); (2) estimated solar radiation data based on geostationary satellite data (Zhao and Duan, 2020); and (3) land surface model output or reanalysis data (Long et al., 2020; Zhou et al., 2021). The methods for reconstructing cloudy-sky Ts include: (1) surface energy balance model (Yu et al., 2019; Zeng et al., 2018); (2) linear regression method (Zhou et al., 2021); (3) machine learning algorithm (Zhao and Duan, 2020; Shwetha and Kumar, 2016; Cho et al., 2022); and (4) spatio-temporal fusion method (Long et al., 2020).

Various methods have been proposed to solve the problem of discontinuity of the in situ Ta data. First, reanalysis Ta data, such as ERA5 (Hersbach et al., 2020) and MERRA-2 (Gelaro et al., 2017) have been developed but have low accuracy and spatial resolution (Rao et al., 2019; Wang and Yan, 2015). Second, some studies have used the weather research and forecast (WRF) model to generate high-resolution Ta data for further research (Li et al., 2019; Ramamurthy and Bou-Zeid, 2017; Ribeiro et al., 2021). However, the WRF model is extremely time consuming, which makes it difficult to generate global Ta data with high spatial resolution. Finally, the Ta data can be mapped using MODIS Ts and in situ Ta data. This method has been successfully used to map Ta at regional and global scales (Hooker et al., 2018; Li et al., 2018b; Lu et al., 2018; Shen et al., 2020).

Based on the aforementioned technologies, various gridded Ts and Ta datasets have been developed (Fick and Hijmans, 2017; Hooker et al.,

Table 1

Data used in this study. Ta: air temperature. Ts: land surface temperature. SURFRAD: Surface Radiation. NCDC: National Climatic Data Center. CMIC: China Meteorological Information Center.

Data	Spatial resolution	Temporal resolution	Source	Time period
NCDC mean Ta	Point	1 day	ftp://ftp.ncdc.noaa.gov/pub/data/gsod/	2001–2020
NCDC maximum Ta	Point	1 day	ftp://ftp.ncdc.noaa.gov/pub/data/gsod/	2001–2020
NCDC minimum Ta	Point	1 day	ftp://ftp.ncdc.noaa.gov/pub/data/gsod/	2001–2020
CMIC mean Ta	Point	1 day	http://data.cma.cn/	2001–2014
CMIC maximum Ta	Point	1 day	http://data.cma.cn/	2001–2014
CMIC minimum Ta	Point	1 day	http://data.cma.cn/	2001–2014
Daytime Ts	1 km	8 days	https://ladsweb.modaps.eosdis.nasa.gov/search/	2001–2020
Nighttime Ts	1 km	8 days	https://ladsweb.modaps.eosdis.nasa.gov/search/	2001–2020
MCD12Q1 land cover	500 m	1 year	https://ladsweb.modaps.eosdis.nasa.gov/search/	2020
MOD11B2	5 km	8 days	https://ladsweb.modaps.eosdis.nasa.gov/search/	2005, 2010 and 2015
Elevation	30 arcsecond	No	Stored in ENVI software	No
Latitude	30 arcsecond	No	Calculated using ArcGIS software	No
Longitude	30 arcsecond	No	Calculated using ArcGIS software	No
ERA5-land Ts	0.1°	1 day	https://www.ecmwf.int/en/forecasts/datasets/reanalysis-datasets/era5	2001–2020
SURFRAD	Point	1–3 min	https://gml.noaa.gov/grad/surfrad/sitepage.html	2005, 2010 and 2015
ERA5 Ta	0.25°	1 month	https://www.ecmwf.int/en/forecasts/datasets/reanalysis-datasets/era5	2001–2020
MERRA2 Ta	0.5° × 0.625°	1 month	https://disc.gsfc.nasa.gov/datasets?project=MERRA-2	2001–2020
HadCRUT5 Ta	5° × 5°	1 month	https://www.metoffice.gov.uk/hadobs/hadcrut5/	2001–2020

2018; Li et al., 2018a; Mata et al., 2019; Metz et al., 2017; Zhao et al., 2020). However, global seamless (without missing values) and high-resolution (30 arcsecond resolution (0.00833°) or higher) Ts and Ta data are still lacking. Some studies have developed seamless Ts data, but only at the regional scale (Li et al., 2018a; Zhao et al., 2020). Metz et al. (2017) developed a global seamless Ts data for the 2003–2016 period, but the spatial resolution was only 3 arcmin (0.05°). Hooker et al. (2018) and Mata et al. (2019) created global Ta data for 2003–2016 and 1983–2016, respectively. However, their spatial resolution was also 3 arcmin. Fick and Hijmans (2017) created a global 30 arcsecond resolution Ta data, but these data were the 31-year (1970–2000) average.

Therefore, the aim of this study was to develop a long-term global seamless and high-resolution temperature (for both Ts and Ta) dataset (GSHTD). First, a method called the estimation of the temperature difference (ETD) was proposed to reconstruct the missing Ts (including both clear- and cloudy-sky Ts) in the MODIS Ts data. The reconstruction

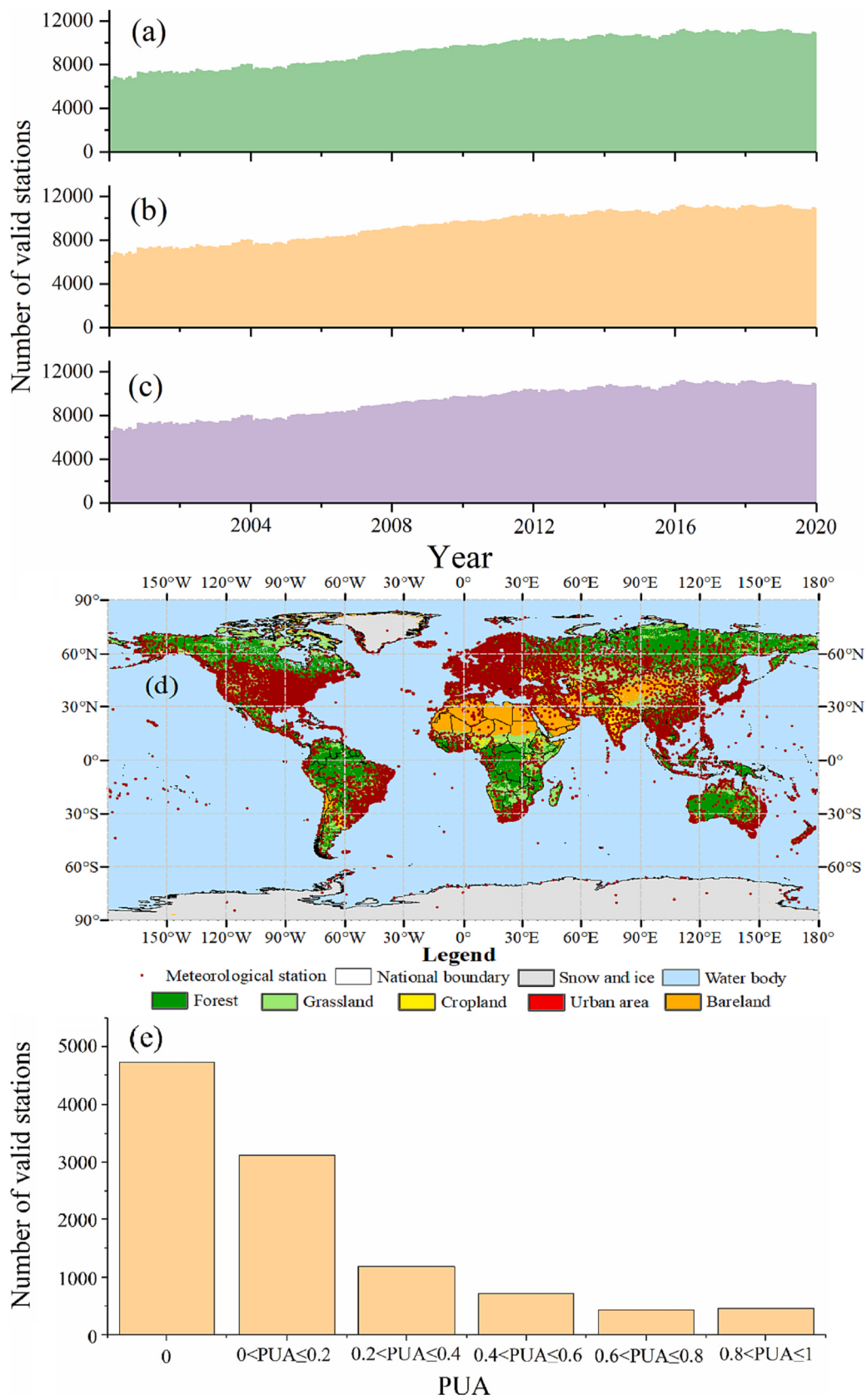


Fig. 1. Number of valid stations. (a) mean air temperature (Ta); (b) maximum Ta; (c) Minimum Ta. (d) Spatial distribution of valid stations in January 2020. The background map is Moderate Resolution Imaging Spectroradiometer (MODIS) MCD12Q1 land cover data. (e) The proportions of urban area (PUA) in 3 km buffer areas around meteorological stations.

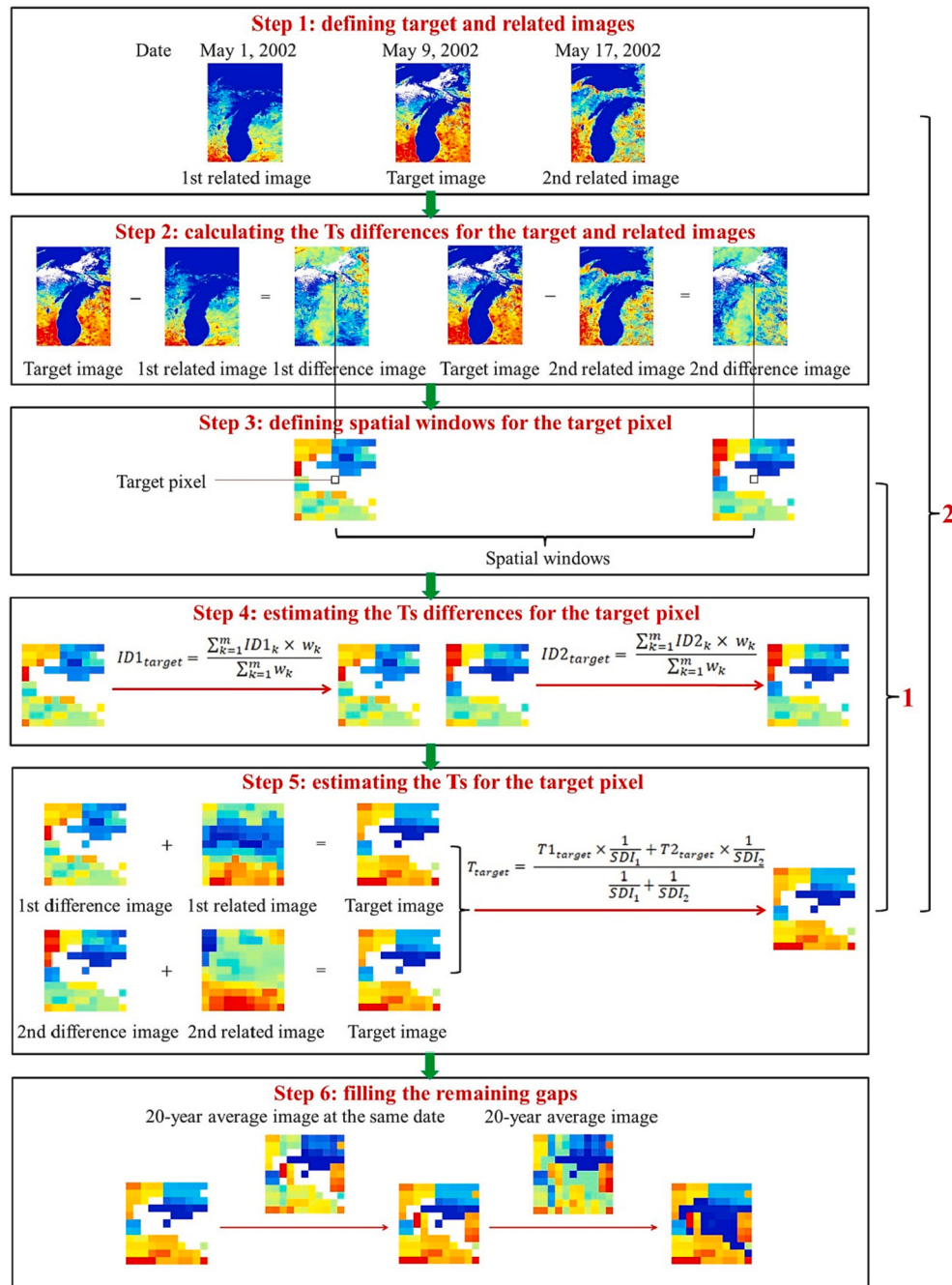


Fig. 2. Schematic of the ETD method. MOD11A2 daytime Ts data on May 9, 2002, was utilized as example.

of clear-sky Ts was validated using artificially created gaps, while the reconstruction of cloudy-sky Ts was verified using in situ measurements. Second, global seamless 8-day and monthly average Ts data (including clear- and all-sky Ts) with 30 arcsecond resolution for the 2001–2020 period were developed using the MODIS Ts data and ETD method. Third, the global seamless monthly average of the mean, maximum and minimum Ta data with 30 arcsecond resolution from 2001 to 2020 were mapped using the Ts data, in situ Ta data and machine learning algorithm.

2. Data and preprocessing

The data used in this work are listed in Table 1. The daily mean, maximum and minimum Ta data were obtained from the Global Surface Summary of Day Product provided by the National Climatic Data Center (NCDC), which conducts strict and extensive quality control. The temporal variations in the number of valid stations are shown in Fig. 1a–1c. The number of valid stations ranges from 6554 to 11,215, with a larger number of valid stations in later years (Fig. 1). These stations are unevenly distributed, with fewer stations in the deserts, mountains and polar regions (Fig. 1d). The proportions of urban area in 3 km buffer areas around meteorological stations were calculated using MCD12Q1

land cover data in 2020 (Fig. 1e). Results showed that most (55.6%) meteorological stations were located in or around urban area, with the proportions of urban area higher than 0%. There was sufficient number of samples (> 400 meteorological stations) in each range of proportions of urban area, which enabled reliable fitting of the relationship between Ta and predictor variables, and estimation of Ta.

Daytime (10: 30 am local solar time) and nighttime (10: 30 pm local solar time) Ts data for the 2001–2020 period were derived from the MODIS MOD11A2 8-day composite product. The elevation information was derived from the global multi-resolution terrain elevation data 2010 (GMTED2010) (Danielson and Gesch, 2011). ERA5-land reanalysis Ts data were used to reconstruct cloudy-sky Ts. SURFRAD data were used to validate the accuracy of reconstructed cloudy-sky Ts. The monthly mean single-level ERA5 (Hersbach et al., 2020) and MERRA2 (assimilation, single-level diagnostics, version 5.12.4) (Gelaro et al., 2017) reanalysis Ta data from 2001 to 2020 were compared with the estimated Ta. The trends of Ta derived from GSHTD, ERA5, MERRA2 and HadCRUT5 (Morice et al., 2021) were compared. The estimated Ta was not directly compared with HadCRUT5, because HadCRUT5 is presented as Ta anomalies relative to 1961–1990.

The daily mean, maximum and minimum Ta were averaged into monthly average of the mean, maximum and minimum Ta. If a station had >7 missing values in a month, the data from that station for that month was excluded (Xu et al., 2018; Yao et al., 2020a). The elevation, latitude and longitude data were assumed to represent the entire study period (2001–2020).

3. Methods

In this work, we first used the ETD method to reconstruct the clear-sky Ts (section 3.1), then combined the ETD method and ERA5-land reanalysis Ts to reconstruct the cloudy-sky Ts (section 3.2). The reconstructed clear-sky Ts was not the real Ts, but it was still reconstructed because: (1) the reconstruction of clear-sky Ts data is an important part of some methods to reconstruct cloudy-sky Ts (Wang et al., 2019; Zeng et al., 2018); and (2) the reconstructed clear-sky Ts data have widely been used in previous studies such as analyzing the surface UHI effect (Liu et al., 2020), mapping Ta data (Leihy et al., 2018; Li et al., 2018b), investigating drought characteristics (Yang et al., 2020) and assessing the relationship between Ts and vegetation (Li et al., 2020).

3.1. The reconstruction of clear-sky Ts

The reconstruction of clear-sky Ts includes six steps (Fig. 2).

(1) Defining the target and related images. The image to be filled was defined as the target image, and two images adjacent to the date of the target image were defined as related images. For example, the related images of the target image on May 9, 2002 were the images on May 1, 2002 and May 17, 2002 (Fig. 2).

(2) Calculating the Ts differences for the target and related images:

$$ID1 = I_{target} - I_{r1} \quad (1)$$

$$ID2 = I_{target} - I_{r2} \quad (2)$$

where $ID1$ and $ID2$ are the Ts difference images, I_{target} is the target image, and I_{r1} and I_{r2} are two related images. If the Ts of a pixel is missing in the target or related image, this pixel in the Ts difference image is treated as missing.

(3) Defining a spatial window for the target pixel. In the target image, the pixel to be filled was defined as the target pixel. A spatial window was generated and its center was set on the target pixel. The size of the spatial window was iteratively increased from 11×11 to 191×191 pixels with an interval of 20×20 pixels (Gerber et al., 2018; Li et al., 2018a; Zeng et al., 2015). The process of increase in the window size was stopped (and the spatial window was chosen for the target

pixel) when there were at least two valid Ts values in the spatial window in at least one Ts difference image. The threshold was selected as two rather than one to include more samples. The maximum size (191×191 pixels) of the window was set to reduce the computing time when filling large gaps (Li et al., 2018a; Zeng et al., 2015). Then, the Ts data in the defined spatial window in the target image, two related images and two difference images were extracted.

(4) Estimating the Ts difference for the target pixel. The value of the target pixel in $ID1$ is estimated as the weighted average value of pixels in the spatial window:

$$ID1_{target} = \frac{\sum_{k=1}^m ID1_k \times w_k}{\sum_{k=1}^m w_k} \quad (3)$$

This equation is based on the hypothesis that the Ts difference of the target pixel will be similar to that of nearby pixels. The Ts difference of the target pixel will be predicted based on this hypothesis. This hypothesis is relatively correct when these two pixels are close in space and have similar surface characteristics. Eq. (3) is a weighted average formula. In this equation, weight of each pixel is normalized to the range of [0,1], and the sum of all weights is 1. $ID1_{target}$ is the value of the target pixel in $ID1$, k is the k th valid pixel in the spatial window in $ID1$, m is the number of valid pixels in the spatial window of $ID1$, and $ID1_k$ is the value of the k th pixel in the spatial window of $ID1$. w_k is the weight of the k th pixel, which is calculated as:

$$w_k = \frac{1}{DI_k^3 \times SI_k^3} \quad (4)$$

where the distance index (DI) (Sun et al., 2017) is calculated as:

$$DI_k = \sqrt{(x_0 - x_k)^2 + (y_0 - y_k)^2} \quad (5)$$

where x_0 and y_0 are the location of the target pixel in $ID1$, and x_k and y_k are the location of the k th valid pixel in the spatial window in $ID1$. The reason for using this index is that nearby pixels generally have close relationships. The similarity index (SI) (Sun et al., 2017) is calculated as:

$$SI_k = |T_{x_0, y_0} - T_{x_k, y_k}| + 1 \quad (6)$$

where T_{x_0, y_0} is the Ts of the target pixel (at location (x_0, y_0)) in the first related image, and T_{x_k, y_k} is the Ts of the k th pixel (at location (x_k, y_k)) in the first related image. The SI was used because pixels with close Ts values normally have similar land cover types or elevations. The value of the target pixel in $ID2$ was estimated using the same method. When the powers of the DI and SI in Eq. (4) were selected as 3, ETD had the highest accuracy (Tables S1 and S2).

(5) Estimating the Ts of the target pixel. The Ts for the target pixel can be estimated as:

$$T1_{target} = TR1_{target} + TD1_{target} \quad (7)$$

$$T2_{target} = TR2_{target} + TD2_{target} \quad (8)$$

where $T1_{target}$ and $T2_{target}$ are the Ts of the target pixel in the target image estimated using the first and second related images, respectively. $TR1_{target}$ and $TR2_{target}$ are the Ts for the target pixel in the first and second related images, respectively. $TD1_{target}$ and $TD2_{target}$ are the values for the target pixel in $ID1$ and $ID2$, respectively. The Ts for the target pixel is estimated as the weighted average of the two estimated Ts values:

$$T_{target} = \frac{T1_{target} \times \frac{1}{SDI_1} + T2_{target} \times \frac{1}{SDI_2}}{\frac{1}{SDI_1} + \frac{1}{SDI_2}} \quad (9)$$

where T_{target} is the final estimated Ts of the target pixel in the target image. $T1_{target}$ and $T2_{target}$ are the Ts of the target pixel in the target image estimated using the first and second related images, respectively, and $\frac{1}{SDI_1}$ and $\frac{1}{SDI_2}$ are weights. The standard deviation index (SDI) is

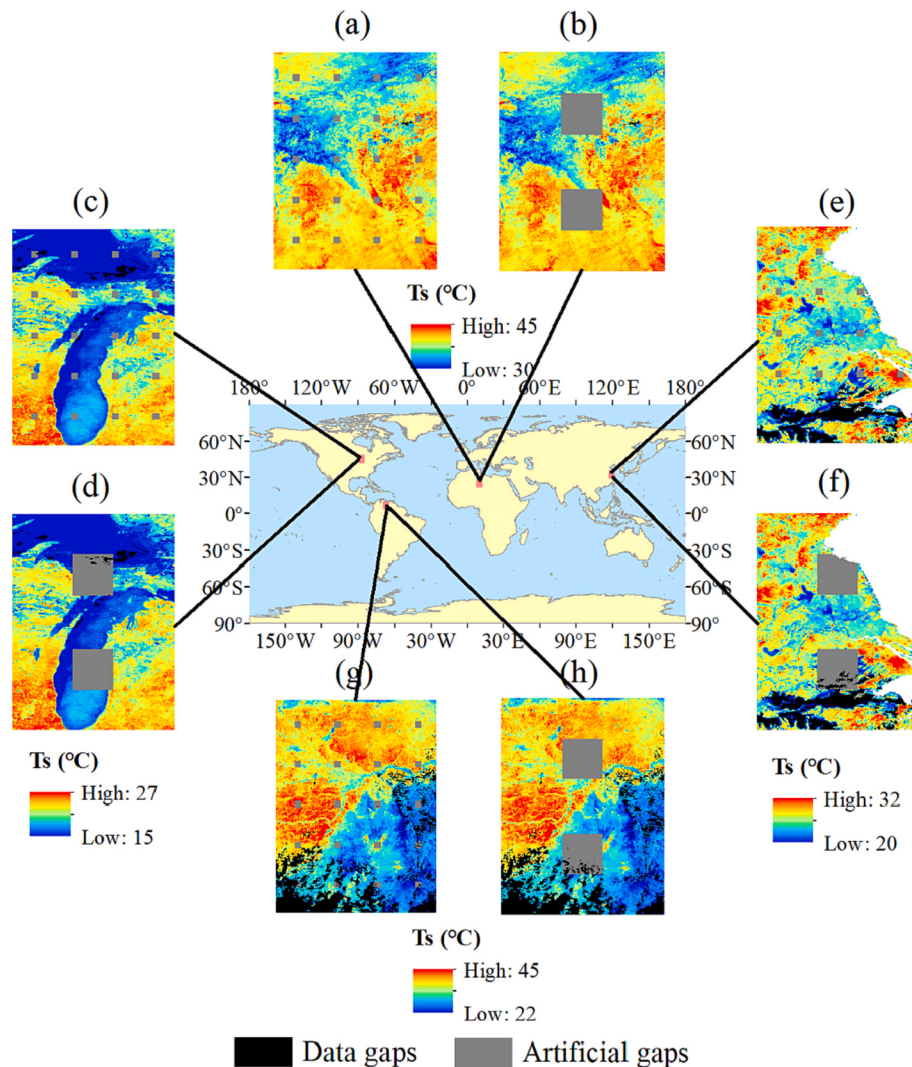


Fig. 3. Examples of artificially created gaps. (a) 20 × 20 pixel gaps in the Sahara Desert. (b) 150 × 150 pixel gaps in the Sahara Desert. (c) 20 × 20 pixel gaps in the Northern United States. (d) 150 × 150 pixel gaps in the Northern United States. (e) 20 × 20 pixel gaps in the Yangtze River Delta. (f) 150 × 150 pixel gaps in the Yangtze River Delta. (g) 20 × 20 pixel gaps in the Amazon Forest. (h) 150 × 150 pixel gaps in the Amazon Forest.

computed as the standard deviation of the Ts difference between the target image and related images in the spatial window (Yao et al., 2021b):

$$SDI_1 = \sqrt{\frac{1}{n1} \times \sum_{r=1}^{n1} (TD_{1,r} - \overline{TD}_1)^2} \quad (10)$$

$$SDI_2 = \sqrt{\frac{1}{n2} \times \sum_{r=1}^{n2} (TD_{2,r} - \overline{TD}_2)^2} \quad (11)$$

where $n1$ and $n2$ are the numbers of valid Ts in the spatial window in $ID1$ and $ID2$, respectively. $TD_{1,r}$ and $TD_{2,r}$ are the values at the r th pixel in the spatial window in $ID1$ and $ID2$, respectively. \overline{TD}_1 and \overline{TD}_2 are the average values in the spatial window in the $ID1$ and $ID2$, respectively. The SDI was used because two images with a lower spatial standard deviation of the Ts difference will have closer relationships (Yao et al., 2021b).

Steps (3)–(5) were repeated to fill all the missing values in the target image. Note that the filled Ts was not used to fill the subsequent pixels. Steps (1)–(5) were repeated to fill all the MOD11A2 8-day composite Ts images for the period 2001–2020. Note that some gaps could not be filled using steps (1)–(5). This occurred: a) when the size of the gaps was large (e.g., exceeding 191 × 191 pixel (see step (3))) and b) when the

pixels in the target, and the first and second related images were all missing. Therefore, steps (1)–(5) were repeated three times to fill more gaps (Li et al., 2018a). At the global scale, 6.72% (6.97%) of the values were missing from 2001 to 2020 in the original daytime (nighttime) Ts images. There were still 1.50% (2.44%), 0.75% (1.50%) and 0.49% (1.06%) of the values missing in the daytime (nighttime) Ts images after implementing steps (1)–(5) one, two and three times, respectively.

(6) Filling the remaining gaps. There were some gaps that were not filled by the aforementioned five steps. 20-year average Ts at the same pixel and date were used to fill these remaining gaps. After this step, <0.01% of the values were missing. All the remaining gaps were finally filled using the 20-year average Ts.

The seamless 8-day composite clear-sky Ts data were generated using the MODIS MOD11A2 Ts data and the ETD method. The 8-day composite Ts data were then averaged into 1-month composite Ts data. Therefore, global seamless 8-day and 1-month composite clear-sky daytime (10:30 am local solar time) and nighttime (10:30 pm local solar time) Ts data with 30 arcsecond resolution from 2001 to 2020 were developed.

3.2. The reconstruction of cloudy-sky Ts

The ETD method and ERA5-land reanalysis Ts data were used to

reconstruct cloudy-sky Ts. This idea is supported by Long et al., (2020) and Zhou et al., (2021). Because the spatial resolution of ERA5-land Ts data is lower than MODIS Ts data, we downsampled the ERA5-land Ts data to 30 arcsecond resolution using the following two steps.

(1) Calculating the Ts differences for the MODIS and ERA5-land images:

$$ID3 = I_{ERA} - I_{MODIS} \quad (12)$$

where I_{ERA} is ERA5-land Ts image. I_{MODIS} is MODIS monthly average reconstructed clear-sky Ts data. The use of monthly average data rather than 8-day average data is to smooth outliers. ID3 is Ts difference image. The spatial resolutions of I_{ERA} and I_{MODIS} were 0.1° and 30 arcsecond (0.00833°), respectively. Therefore, one pixel in ERA-land data corresponds to 144 (12×12) pixels in MODIS data. The Ts differences were calculated as ERA5-land Ts minus 144-pixel average MODIS Ts. ID3 was then directly resampled to 30 arcsecond resolution.

(2) Developing downscaled ERA5-land Ts images:

$$D_{ERA} = ID3_R + I_{MODIS} \quad (13)$$

where D_{ERA} is downscaled ERA5-land Ts image, $ID3_R$ is resampled Ts difference image. Because MODIS Ts data can reflect the heterogeneity of the underlying land surface within a 0.1° grid, so can the downscaled ERA5-land Ts. This is based on the hypothesis that the spatial variations in Ts of MODIS data is the same as that of ERA5-land data. The coarse resolution data were directly resampled to 1 km resolution, and then used to reconstruct cloudy-sky Ts in some previous studies (Zhou et al., 2021; Long et al., 2020). The downscaling method in this study is more reliable than that in previous studies.

The downscaled ERA5-land Ts data were used to reconstruct cloudy-sky Ts. Necessary modifications to ETD method mentioned in previous section were made to reconstruct cloudy-sky Ts. First, in the first step of ETD, the related image of the target image was defined as the ERA5-land Ts data at the same date and time. Second, in the third step of ETD, the maximum size of spatial window was not set. Therefore, all gaps can be filled at once. Third, in the fourth step of ETD, the DI was not used and the power of SI was set as 1 according to test results (Table S3). Fourth, in the fifth step of ETD, the SDI was not used, because there was only one related image (ERA5-land Ts data at the same date and time) for the target image.

The original MOD11A2 is 8-day composite clear-sky Ts data with 30 arcsecond resolution. The missing values were filled with cloudy-sky Ts using ETD method. Therefore, seamless 8-day composite all-sky Ts data from 2001 to 2020 were developed. Then, the 8-day composite Ts data were averaged into 1-month composite Ts data.

3.3. Accuracy verification of gapfilling

The accuracy of ETD in reconstructing clear-sky Ts was tested in four areas with 600×800 pixels: the Sahara Desert, Northern United States, Yangtze River Delta and Amazon Forest (Fig. 3). These four areas were selected because they represent different land cover and landscape types. The Sahara Desert, Northern United States, Yangtze River Delta and Amazon Forest represent bare land, water bodies, urban areas and vegetation, respectively. Gaps of 25×25 and 150×150 pixels were artificially created in the 2nd, 5th, 8th, 11th, 14th, 17th, 20th, 23rd, 26th, 29th, 32nd, 35th, 38th, 41st and 44th images (i.e., selecting one image for every three images) in 2005, 2010 and 2015 (see examples in Fig. 3). Then, the artificial gaps were filled with the ETD method. Subsequently, the filled Ts values were compared with the observed Ts values. The mean absolute error (MAE), root mean square error (RMSE) and coefficient of determination (R^2) were utilized to assess the accuracy. The accuracy of ETD method in reconstructing daily Ts data was also validated using daily MODIS Ts data at the same date. The use of original Ts to validate the reconstructed clear-sky Ts is the same as many previous studies (Li et al., 2018a; Militino et al., 2019a; Militino et al.,

2019b; Yao et al., 2021b; Gerber et al., 2018; Sun et al., 2017). Note that the reconstructed clear-sky Ts should not be compared with the in situ Ts data. This is because this study reconstructed the clear-sky (unreal) Ts under cloudy conditions, whereas the in situ Ts data is real Ts under cloudy conditions.

The accuracy of ETD in reconstructing cloudy-sky Ts was validated using Surface Radiation (SURFRAD) in situ measurements and MODIS Ts data in 2005, 2010 and 2015. SURFRAD stations measured the surface radiation for every 1 or 3 min. A transformation was implemented to convert surface longwave radiation to Ts according to previous studies (Duan et al., 2017; Zeng et al., 2018; Liu et al., 2019; Long et al., 2020):

$$T_s = \left(\frac{L_\uparrow - (1 - \varepsilon_b) \times L_\downarrow}{\varepsilon_b \sigma} \right)^{\frac{1}{4}} \quad (14)$$

where L_\uparrow and L_\downarrow are upwelling and downwelling longwave radiation, respectively. They were derived from SURFRAD in situ measurements. σ is the Stefan-Boltzmann constant, which equals to $5.67 \times 10^{-8} \text{ W m}^{-2} \text{ K}^{-4}$. ε_b is the surface broadband emissivity, which was estimated from MOD11B2 emissivity data (Wang and Liang, 2009; Duan et al., 2017):

$$\varepsilon_b = 0.2122 \times \varepsilon_{29} + 0.3859 \times \varepsilon_{31} + 0.4029 \times \varepsilon_{32} \quad (15)$$

where ε_{29} , ε_{31} and ε_{32} are the narrowband emissivity data in MOD11B2 product.

3.4. Accuracy comparison of gapfilling

The accuracy of ETD in reconstructing clear-sky Ts was compared with Remotely Sensed DAily land Surface Temperature reconstruction (RSDAST) (Sun et al., 2017) and interpolation of the mean anomalies (IMAs) (Militino et al., 2019b). RSDAST first defines a temporal subset and a stationary 9×9 spatial window for a missing Ts. It then predicts the missing Ts as the weighted average of the Ts of the target pixel in another image minus Ts of the nearby pixels in another image and plus the Ts of the nearby pixels in the same image. DI and SI are used to weight predicted Ts. The filled Ts is then considered a valid value when filling other pixels (Sun et al., 2017). IMA first defines a temporal subset, and then calculates the mean image of the subset and the anomaly image (target image minus mean image). Subsequently, thin plate spine interpolation method is used to fill the gaps in the anomaly image. The final gapfilled image is calculated as the interpolated anomaly image adds the mean image (Militino et al., 2019b).

There are two main reasons for selecting these two methods. First, these two methods have higher proven accuracy than other methods. RSDAST outperforms Gapfill (Yao et al., 2021b) and regression kriging (Liu et al., 2019). IMA performs better than Gapfill, harmonic analysis of time series and TIMESAT software (Militino et al., 2019b; Yao et al., 2021b). Second, RSDAST and IMA are easy to use. RSDAST is relatively simple and, therefore, has been widely used (Liu et al., 2019; Yang et al., 2020; Yao et al., 2021b). IMA can be conveniently run with the “RGISTool” add-on package in the R statistical software.

3.5. Processing times of gapfilling methods

The processing times of the three methods were tested using ten MOD11A2 daytime Ts images from March 30, 2017, to June 10, 2017, in the Amazon Forest (600×800 pixels). These images were selected because the proportions of valid Ts to the entire image were relatively evenly distributed between 0% and 100%. These analyses were performed using a personal computer with an Intel Core i7-8700 CPU and 16 GB RAM.

3.6. Ta estimation

The Ta estimation includes the following three steps, which are

Table 2

Accuracies of three methods in filling 25×25 pixel gaps in 8-day composite MOD11A2 Ts data. ETD: estimation of the temperature difference. RSDAST: Remotely Sensed DAily land Surface Temperature. IMA: interpolation of the mean anomalies. MAE: mean absolute error. RMSE: root mean square error. R^2 : coefficient of determination.

	ETD		RSDAST		IMA	
	Daytime	Nighttime	Daytime	Nighttime	Daytime	Nighttime
Amazon Forest						
MAE (°C)	0.920	0.539	1.076	0.685	1.174	0.722
RMSE (°C)	1.329	0.890	1.527	1.122	1.655	1.222
R^2	0.942	0.869	0.923	0.799	0.910	0.754
Northern United States						
MAE (°C)	0.768	0.729	0.931	0.902	1.138	1.048
RMSE (°C)	1.240	1.283	1.451	1.516	1.818	1.518
R^2	0.989	0.982	0.985	0.975	0.976	0.967
Sahara Desert						
MAE (°C)	0.459	0.404	0.565	0.491	0.608	0.525
RMSE (°C)	0.708	0.663	0.821	0.764	0.884	0.819
R^2	0.994	0.992	0.992	0.989	0.990	0.988
Yangtze River Delta						
MAE (°C)	0.750	0.535	0.917	0.694	1.034	0.781
RMSE (°C)	1.190	0.892	1.401	1.089	1.562	1.222
R^2	0.984	0.992	0.978	0.988	0.973	0.984
Average						
MAE (°C)	0.724	0.552	0.872	0.693	0.989	0.769
RMSE (°C)	1.117	0.932	1.300	1.123	1.480	1.195
R^2	0.977	0.959	0.970	0.938	0.962	0.923

described in this paragraph. Model and variable selections can be found in the next paragraph. First, the values of the pixels corresponding to the location of the meteorological station were extracted from the daytime and nighttime Ts data. If a weather station was located between two or four pixels, the average values of these two or four pixels were used. The year, DEM, latitude and longitude data from meteorological stations were directly employed. Second, these predictor variables and Ta were input into the Cubist model. In this study, data in different months were input into the model separately, because this strategy can concentrate samples with similar characteristics (e.g., meteorological and environmental conditions) and improve the accuracy of the estimated Ta (Yao et al., 2020a). In each month, all samples were used, to ensure a sufficient number of samples (Yoo et al., 2018; Stisen et al., 2007). The relationship between the predictor variables and Ta was fitted using the Cubist model for each month for the whole globe. Third, monthly Ta for each pixel can be predicted using the fitted relationship and predictor variable data of corresponding pixel. When the Ta of all pixels is predicted, gridded global Ta data can be developed (Rosenfeld et al., 2017;

Hereher and El Kenawy, 2020; Gao et al., 2021).

The Cubist machine learning algorithm originates from the M5 model tree, and is a rule-based regression model. Originally, Cubist is a commercial software, but it currently can be performed through “Cubist” add-on package in R statistical software. It was used to estimate the Ta in this study, because previous works demonstrated that the accuracy of Cubist was higher than that of other algorithms (Xu et al., 2018; Zhang et al., 2016; Noi et al., 2017; Zhang et al., 2020). For example, Xu et al., (2018) used ten machine learning algorithms to estimate monthly Ta, and found that Cubist had the highest accuracy (RMSE: 0.99 °C). Zhang et al., (2016) used six models to estimate daily Ta, and found that Cubist and random forests performed best (RMSE: approximately 2 °C). Parameter of Cubist model was selected using “caret” add-on package in R software. The daytime Ts, nighttime Ts, DEM, latitude, longitude and year were used as predictor variables to estimate the Ta because the test results showed that they can improve the accuracy of Ta estimation (see Section 4.2).

Table 3

Accuracies of three methods in filling 150×150 pixel gaps in MOD11A2 Ts data.

	ETD		RSDAST		IMA	
	Daytime	Nighttime	Daytime	Nighttime	Daytime	Nighttime
Amazon Forest						
MAE (°C)	1.254	0.992	1.602	1.253	1.593	1.195
RMSE (°C)	1.759	1.613	2.454	1.957	2.190	1.887
R^2	0.907	0.774	0.830	0.684	0.865	0.705
Northern United States						
MAE (°C)	1.047	1.096	1.536	1.850	1.377	1.474
RMSE (°C)	1.632	1.862	2.357	2.920	2.072	2.307
R^2	0.974	0.959	0.945	0.898	0.958	0.937
Sahara Desert						
MAE (°C)	0.721	0.611	0.944	0.778	0.913	0.789
RMSE (°C)	1.023	0.899	1.301	1.106	1.296	1.129
R^2	0.987	0.985	0.978	0.977	0.979	0.977
Yangtze River Delta						
MAE (°C)	1.072	0.880	1.611	1.338	1.464	1.227
RMSE (°C)	1.562	1.348	2.400	1.912	2.042	1.767
R^2	0.971	0.981	0.932	0.961	0.951	0.967
Average						
MAE (°C)	1.024	0.895	1.423	1.305	1.337	1.171
RMSE (°C)	1.494	1.431	2.128	1.974	1.900	1.773
R^2	0.960	0.925	0.921	0.880	0.938	0.897

3.7. Accuracy assessment of Ta estimation

A leave-station-out 10-fold cross-validation method was used to test the accuracy of the estimated Ta. All meteorological stations were divided into ten parts. Samples from nine subsets of stations were used for training, and samples from the remaining one subset of stations were used for validation. This step was repeated ten times, with each subset of stations used to test the accuracy once. MAE, RMSE and R^2 were utilized to assess the accuracy (Xu et al., 2018; Yoo et al., 2018).

The leave-station-out 10-fold cross-validation method is more reasonable than the leave-sample-out 10-fold cross-validation method. The purpose of this paper is to estimate the Ta in areas without meteorological stations, and finally develop a Ta map. The validation scenario should be close to the actual estimation scenario. In the validation process of leave-station-out 10-fold cross-validation method, the stations used for validation were not used for training. This is consistent with the actual estimation scenario (estimating the Ta in areas without meteorological stations). In the validation process of leave-sample-out 10-fold cross-validation method, this situation may occur: data from one date of a station is used for training and data from another date of the same station is used for verification. This situation is not consistent with the actual estimation scenario. Therefore, leave-station-out 10-fold cross-validation method was used rather than leave-sample-out 10-fold cross-validation method.

The daily mean, maximum and minimum Ta derived from China Meteorological Information Center (CMIC) were used as an independent dataset to validate the accuracy of Ta estimation (Table 1). This dataset is available from 2001 to 2014, which contains 2474 meteorological stations in China. The use of an independent dataset for validation can provide more thorough and objective validation results.

4. Results

4.1. Accuracies and processing times of Ts reconstruction

4.1.1. Reconstruction of clear-sky Ts

The accuracy of ETD was significantly higher than that of the other two gapfilling methods (Tables 2, 3, S4 and S5). The average MAEs of ETD, RSDAST and IMA in filling 25×25 pixel gaps in the 8-day composite daytime (nighttime) Ts data were 0.724 (0.552), 0.872 (0.693) and 0.989 (0.769) °C, respectively. The average MAEs of ETD, RSDAST and IMA in filling 150×150 pixel gaps in the 8-day composite daytime (nighttime) Ts data were 1.024 (0.895), 1.423 (1.305) and 1.337 (1.171) °C, respectively. The MAEs of ETD were 14.1–31.4% (average: 23.2%) lower than that of RSDAST and 19.3–28.3% (average: 23.7%) lower than that of IMA. Additionally, ETD outperformed RSDAST and IMA in all four study areas, for both small and large gaps, and for both daytime and nighttime Ts. These results suggest that ETD is a robust gapfilling method.

RSDAST has lower accuracy compared to the ETD, primarily due to following two reasons. The first reason is that RSDAST uses filled Ts to fill other missing values (Sun et al., 2017). Therefore, error propagation widely exists in images filled with RSDAST, especially in images with large gaps. For example, the accuracy of RSDAST in filling 25×25 pixel gaps was higher than that of the IMA, while opposite result was found when filling 150×150 pixel gaps (Tables 2 and 3). For the ETD method, error propagation exists in the second and third round of gapfilling, but not in the first round of gapfilling. The first round of gapfilling can fill majority of the gaps (see section 3.1). Therefore, most filled Ts will not be affected by error propagation. The second reason is that ETD method uses the optimal powers of DI and SI. Comparatively, the powers in RSDAST (Sun et al., 2017), as well as some previous methods (Long et al., 2020; Zeng et al., 2018; Zeng et al., 2015; Zhu et al., 2010) were all directly set as 1. Further analysis showed that the powers of DI and SI have great influence on accuracy of gapfilling (Tables S1, S2 and S3). For example, the MAE of ETD in filling 25×25 pixel gaps in daytime Ts data

Table 4
Processing times of the three methods.

Julian day	Proportion of valid value	ETD (Unit: second)	RSDAST (Unit: second)	IMA (Unit: second)
89	98.7%	4	1	7084
97	86.0%	21	3	11,460
105	70.3%	34	4	3732
113	75.4%	18	3	3808
121	28.3%	135	9	585
129	17.3%	138	10	298
137	83.5%	12	2	3015
145	59.1%	50	6	2776
153	46.5%	54	6	1267
161	39.8%	50	7	1266
Total		516	51	35,291

was 0.789 °C when the powers of DI and SI were all set as 1, while the MAE was 0.724 °C when the powers of DI and SI were all set as 3. The low accuracy of the IMA can be attributed to two predominant reasons. First, IMA calculates a multi-day average image around the target image. However, this step may cause some uncertainties because there are some gaps in the original Ts images. Second, IMA uses a 5×5 pixel average method to smooth images. This strategy can reduce the computing costs but increase errors (Militino et al., 2019b).

The accuracies of reconstructing the daytime Ts were lower than those of reconstructing the nighttime Ts. This is mainly because the daytime Ts is significantly affected by solar radiation, vegetation cover and land cover types, and is more variable than the nighttime Ts (Peng et al., 2012; Yao et al., 2021b; Yoo et al., 2018). Therefore, daytime Ts is harder to predict than nighttime Ts. Additionally, the accuracies of reconstructing 25×25 pixel gaps were higher than those of reconstructing 150×150 pixel gaps. This result was understandable because large gaps were filled using distant pixels, which may have relatively weak relationships with the target pixel. Furthermore, the accuracy of the reconstruction of daily Ts was not necessarily lower than that of the reconstruction of 8-day composite Ts (Tables S4 and S5). The 8-day composite product is the average of daily product. Missing values were not used in the average procedure. Therefore, the original 8-day composite Ts data have some uncertainties. Finally, the accuracies of filling the gaps in the Sahara Desert were higher than in other areas. This can be attributed to two reasons. First, the land cover type in the Sahara Desert is homogeneous. Second, there are few clouds in the Sahara Desert, and the proportion of valid pixels is high. Therefore, the valid Ts closer to the target pixel in time and space can be used to fill the target pixel.

The processing times of the three gapfilling methods are listed in Table 4. RSDAST ranked first. The reason for the less processing time of RSDAST is that it uses filled Ts to fill other missing values (Sun et al., 2017). Therefore, large gaps can be rapidly filled based on this strategy. ETD ranked second. Although the processing time of ETD was significantly higher than that of RSDAST, it was acceptable and lower than that of IMA. IMA ranked last, because the thin plate spline interpolation is time consuming. Finally, an interesting phenomenon was that the processing time of IMA decreased when the proportion of valid values decreased. This is because the processing time of thin plate spline interpolation method decreased when the proportion of valid values decreased (Militino et al., 2019b). Overall, ETD is an advanced method with high accuracy and acceptable computing costs.

4.1.2. Reconstruction of cloudy-sky Ts

The ETD method produced an acceptable accuracy of reconstruction of cloudy-sky Ts. The RMSEs of reconstruction of cloudy-sky daytime and nighttime Ts were 5.355 and 5.420 °C, respectively. This accuracy is generally similar to some previous studies that validated with SURFRAD data (RMSEs generally between 4 and 7 °C) (Zeng et al., 2018; Wang et al., 2019; Yu et al., 2022). The accuracy of the reconstructed cloudy-sky Ts was much lower than that of the reconstructed clear-sky Ts. The

Table 5

Accuracies of ETD in reconstructing cloudy-sky Ts.

	Original Ts		Reconstructed cloudy-sky Ts	
	Daytime	Nighttime	Daytime	Nighttime
MAE (°C)	3.019	3.091	3.973	4.073
RMSE (°C)	4.014	3.807	5.355	5.420
R ²	0.919	0.940	0.814	0.789

Table 6

Impacts of daytime Ts, nighttime Ts, elevation, latitude, longitude and year on the accuracy of Ta estimation averaged for January and July.

	Mean Ta	Maximum Ta	Minimum Ta	Average
Using all six variables				
MAE (°C)	0.837	1.022	1.074	0.977
RMSE (°C)	1.265	1.487	1.527	1.426
R ²	0.983	0.978	0.976	0.979
Using clear-sky Ts rather than all-sky Ts				
MAE (°C)	0.838	1.023	1.075	0.979
RMSE (°C)	1.270	1.490	1.527	1.429
R ²	0.983	0.978	0.976	0.979
Do not use all-sky daytime Ts				
MAE (°C)	0.871	1.109	1.088	1.023
RMSE (°C)	1.316	1.627	1.554	1.499
R ²	0.982	0.973	0.975	0.977
Do not use all-sky nighttime Ts				
MAE (°C)	0.930	1.042	1.227	1.066
RMSE (°C)	1.385	1.533	1.733	1.550
R ²	0.980	0.976	0.968	0.974
Do not use elevation				
MAE (°C)	0.924	1.110	1.154	1.062
RMSE (°C)	1.395	1.633	1.638	1.555
R ²	0.979	0.973	0.971	0.974
Do not use latitude				
MAE (°C)	1.014	1.206	1.276	1.165
RMSE (°C)	1.501	1.713	1.809	1.674
R ²	0.975	0.969	0.963	0.969
Do not use longitude				
MAE (°C)	1.066	1.319	1.323	1.236
RMSE (°C)	1.554	1.850	1.859	1.754
R ²	0.976	0.965	0.965	0.969
Do not use year				
MAE (°C)	1.002	1.196	1.229	1.142
RMSE (°C)	1.440	1.676	1.702	1.606
R ²	0.980	0.973	0.971	0.974

errors of reconstruction of cloudy-sky Ts mainly come from: (1) error of original MODIS Ts data. (2) Discrepancy between SURFRAD point Ts and MODIS raster Ts data. It was found that the RMSEs between SURFRAD Ts and original daytime and nighttime MODIS Ts data were 4.014 and 3.807 °C, respectively (Table 5). (3) inconsistency between ERA5-land Ts and MODIS Ts data. Further analysis showed that the average spatial R² and bias between ERA5-land Ts and MODIS Ts in 2020 were 0.953 and 1.748 °C, respectively.

4.2. Accuracies of Ta estimation

Each predictor variable was tested one by one to see whether it can improve the accuracy of Ta estimation. If not, it will not be used to estimate the Ta. Only predictor variables that significantly improve the accuracy of Ta estimation were retained; these included all-sky daytime and nighttime Ts, DEM, latitude, longitude and year (Table 6). For example, the average MAEs of using and not using all-sky nighttime Ts were 0.977 and 1.066 °C, respectively. The reason for the positive impacts of these variables on Ta estimation is that they closely correlate with Ta or affect the relationships between Ta and other predictor variables. Additionally, the accuracy of estimated Ta using all-sky Ts was slightly higher than that of using clear-sky Ts. This is probably because the reconstructed cloudy-sky Ts is closer to the real Ts. Finally, the clear-sky daytime and nighttime Ts, enhanced vegetation index (in MODIS

Table 7

The impacts of clear-sky daytime Ts, clear-sky nighttime Ts, clear-sky days, clear-sky nights, enhanced vegetation index (EVI), slope, aspect and topographic index on the accuracy of Ta estimation averaged for January and July.

	Mean Ta	Maximum Ta	Minimum Ta	Average
Using six variables				
MAE (°C)	0.837	1.022	1.074	0.978
RMSE (°C)	1.265	1.487	1.527	1.426
R ²	0.983	0.978	0.976	0.979
Adding clear-sky daytime Ts				
MAE (°C)	0.849	1.034	1.087	0.990
RMSE (°C)	1.277	1.510	1.550	1.445
R ²	0.983	0.977	0.975	0.978
Adding clear-sky nighttime Ts				
MAE (°C)	0.845	1.035	1.084	0.988
RMSE (°C)	1.270	1.514	1.539	1.441
R ²	0.983	0.977	0.975	0.978
Adding clear-sky days				
MAE (°C)	0.841	1.010	1.083	0.978
RMSE (°C)	1.269	1.466	1.535	1.423
R ²	0.984	0.979	0.976	0.979
Adding clear-sky nights				
MAE (°C)	0.846	1.026	1.085	0.986
RMSE (°C)	1.267	1.492	1.538	1.432
R ²	0.984	0.978	0.975	0.979
Adding EVI				
MAE (°C)	0.859	1.046	1.095	1.000
RMSE (°C)	1.283	1.511	1.549	1.448
R ²	0.983	0.977	0.975	0.978
Adding slope				
MAE (°C)	0.859	1.050	1.095	1.001
RMSE (°C)	1.292	1.527	1.556	1.458
R ²	0.983	0.976	0.975	0.978
Adding aspect				
MAE (°C)	0.903	1.103	1.145	1.050
RMSE (°C)	1.339	1.586	1.612	1.512
R ²	0.982	0.975	0.973	0.976
Adding topographic index				
MAE (°C)	0.894	1.086	1.121	1.033
RMSE (°C)	1.329	1.571	1.587	1.495
R ²	0.982	0.975	0.974	0.977

MOD13A3 product), clear-sky days and nights (in MODIS MOD11A2 product), aspect and slope (calculated using ArcGIS), and topographic index (Matthews et al., 2015) were tested but not used because they did not improve the accuracy of Ta estimation (Table 7).

The estimated Ta had high accuracy with MAEs from 0.708 to 1.187 °C, RMSEs from 1.079 to 1.693 °C, and R² from 0.965 to 0.991 (Fig. 4 and Table 8). The accuracy of the estimated monthly average of mean Ta was higher than that of maximum and minimum Ta. The average MAEs of the estimated monthly average of the mean, maximum and minimum Ta were 0.797, 0.994 and 1.056 °C, respectively (Table 8). This result, which is similar to those of previous studies, is because extreme Ta values are harder to predict (Benali et al., 2012; Yao et al., 2021a). The accuracy of estimated Ta was also validated using an independent Ta dataset derived from 2474 meteorological stations of CMIC (Table 8). The accuracies of estimated mean Ta validated by the two datasets were similar. However, the accuracies of estimation of maximum and minimum Ta validated using CMIC were lower than using NCDC, probably because the observing practices of CMIC and NCDC were different. CMIC uses autonomous weather station system to monitor Ta (Ren et al., 2014), while a large proportion of NCDC stations measure Ta every hour.

Seasonally, the MAEs and RMSEs were normally lower in the Northern Hemisphere summer, and the R² was also lower (Fig. 4). MAE, RMSE and R² are strongly related to the standard deviation of the samples. We have calculated the standard deviation of observed Ta for each month. It can be clearly seen that higher standard deviation of observed Ta are usually accompanied by lower R² and higher MAE and RMSE (e.g., in December, January and February), and vice versa (Figs. 4 and 5). The reason for the low standard deviation of observed Ta in

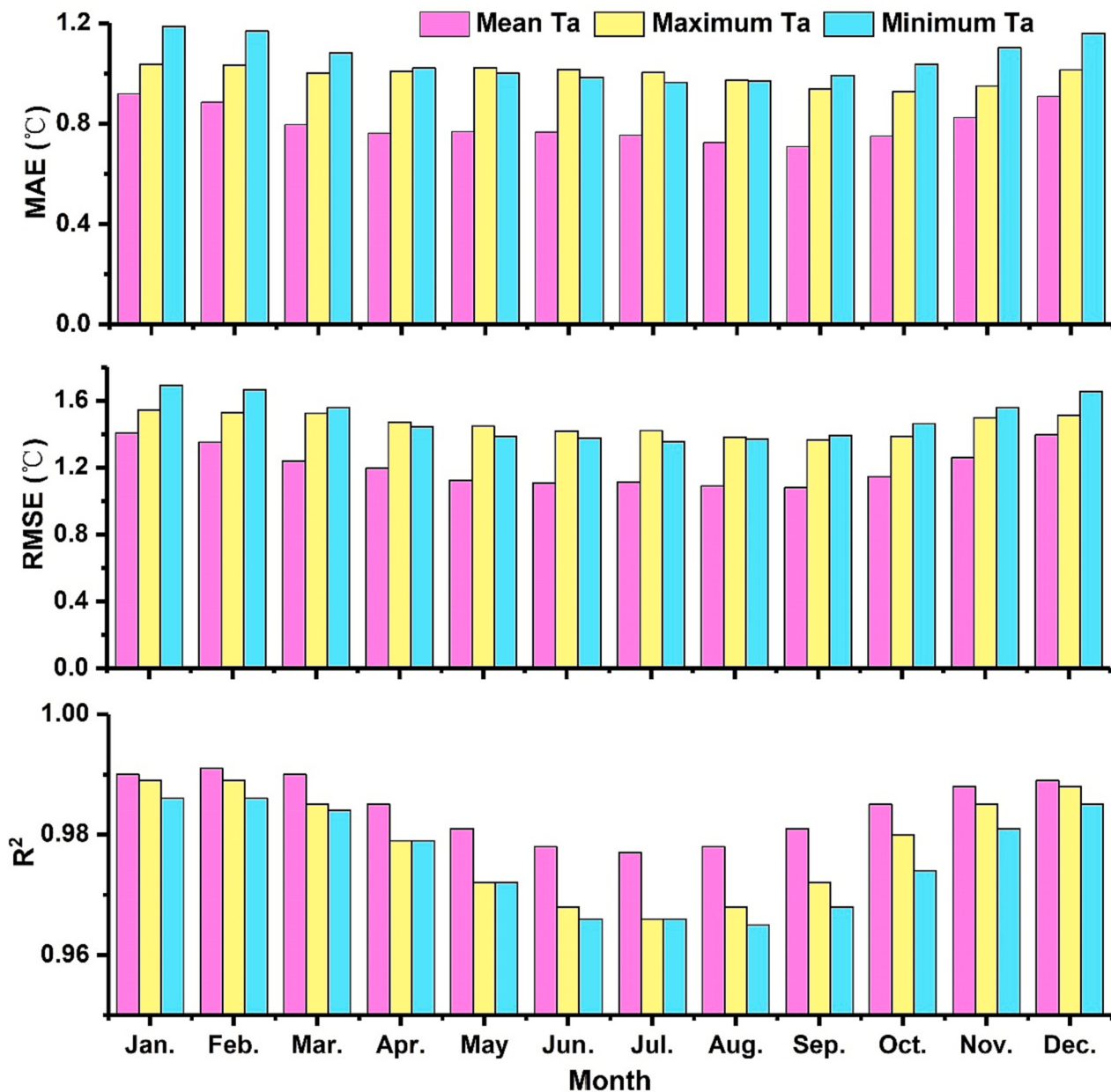


Fig. 4. Accuracies of the estimated Ta validated using 10-fold cross-validation and NCDC Ta data. MAE: mean absolute error. RMSE: root mean square error. R²: coefficient of determination.

Table 8

Accuracy of estimated Ta validated using National Climatic Data Center (NCDC) and China Meteorological Information Center (CMIC).

	Mean Ta	Maximum Ta	Minimum Ta	Average
Validated using NCDC				
MAE (°C)	0.797	0.994	1.056	0.949
RMSE (°C)	1.209	1.458	1.493	1.387
R^2	0.984	0.978	0.976	0.980
Validated using CMIC				
MAE (°C)	0.770	1.373	1.105	1.083
RMSE (°C)	1.056	2.223	1.516	1.598
R^2	0.991	0.959	0.984	0.978

summer months is that most stations are located in the Northern Hemisphere, the differences in Ta between meteorological stations are smaller (i.e., standard deviation of Ta was lower) in the Northern Hemisphere summer than in the Northern Hemisphere winter. In other

words, Ta is latitudinally more similar and more affected by local scale variability in Northern hemisphere summer compared to winter. Therefore, the estimated Ta has lower errors (MAE and RMSE) and a weaker relationship (R^2) with the observed Ta in the Northern Hemisphere summer. Spatially, the MAEs were generally higher in polar regions (e.g., northern Canada, northeastern Russia, Greenland and Antarctica) (Fig. 6). For example, the MAEs in nearly all the meteorological stations were higher than 1 °C in Antarctica. This result is similar to that of Hooker et al. (2018). A possible reason for this is that the meteorological stations are sparsely distributed in these regions. Therefore, few samples were used to train the model, and the relationships between Ta and the predictor variables could not be accurately fitted in these regions. Additionally, the estimation accuracies in the Middle East, Central and North Asia were generally lower (yellow, orange and red dots in Fig. 6). This may also be attributed to sparse distribution of meteorological stations in these regions. The main land cover type in the Middle East and Central Asia is desert, and the North

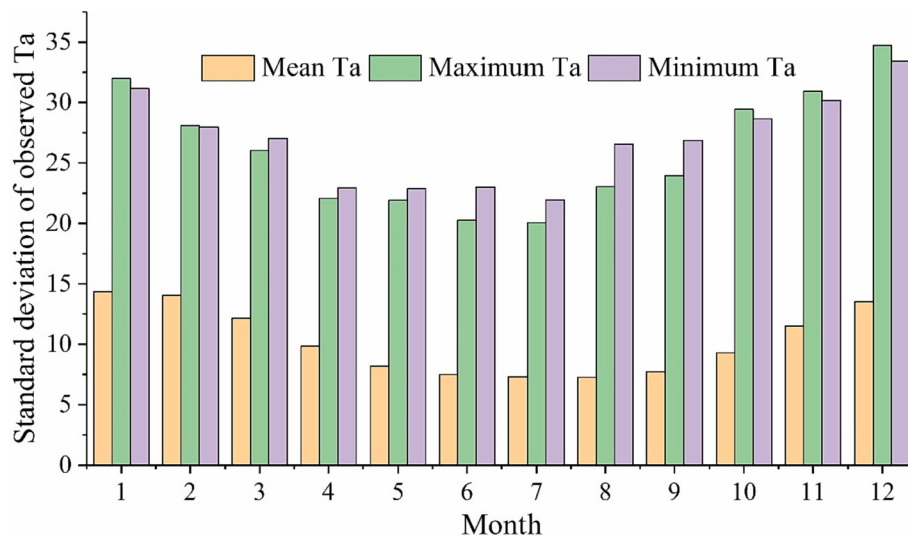


Fig. 5. Standard deviation of observed Ta for each month.

Asia is close to the Arctic.

4.3. Spatio-temporal variations in Ts and Ta

The global seamless 8-day and monthly mean Ts data (including both all- and clear-sky) with 30 arcsecond resolution from 2001 to 2020 were created using the MODIS Ts data and the ETD method. The global seamless monthly average of mean, maximum and minimum Ta data with 30 arcsecond resolution from 2001 to 2020 was developed using in situ Ta data, six predictor variables and the Cubist machine learning algorithm.

The spatial variations in Ts and Ta averaged from 2001 to 2020 are shown in Fig. 7. Spatially, the Ts and Ta were generally low in areas with high latitude (e.g., Antarctica) or elevation (e.g., the Qinghai-Tibet Plateau). Among the seven types of temperatures, the daytime Ts was higher than the other types of temperatures in drylands (e.g., Sahara Desert) (Fig. 7). This is because drylands have limited water content and low heat capacity. Thus, solar radiation during the daytime can heat the surface of the drylands and raise its Ts rapidly. However, the Ts was lower than the Ta in polar regions (e.g., Greenland and Antarctica). This can mainly be attributed to: (1) more surface energy emission than absorption from the Sun and the atmosphere; and (2) advection of warm air masses over a cooler surface layer (Bradley et al., 1992; Zhang et al., 2011).

Fig. 8 shows the comparison among GSHTD, ERA5 and MERRA2 mean Ta in Qinghai-Tibet Plateau. GSHTD can accurately reflect the changes in Ta caused by terrain variations, primarily because of its high spatial resolution. The correlation coefficients between elevation and GSHTD and ERA5 and MERRA2 were -0.924 , -0.728 and -0.816 , respectively. Mean Ta of ERA5 and MERRA2 were more homogenous than that of GSHTD, due to their low spatial resolution. The standard deviation of mean Ta of GSHTD, ERA5 and MERRA2 were 4.532 , 4.485 and 4.362 $^{\circ}\text{C}$, respectively. Spatial distributions of GSHTD, ERA5 and MERRA2 mean Ta and land cover types in Beijing (China) and its surrounding area are presented in Fig. 9. The GSHTD mean Ta could well resolve the UHI effect. It can be clearly seen that the GSHTD mean Ta generally decreased from urban center to rural areas. The GSHTD mean Ta in urban center was approximately 2 $^{\circ}\text{C}$ higher than that in surrounding croplands. Comparatively, there was no significant difference in ERA5 and MERRA2 mean Ta between urban and rural areas.

The global average temperatures increased for the period 2001–2020 (Fig. 10). Interannually, there were strong correlations between all the temperatures. These temperatures were generally higher in 2016 and 2020 than in other years. For the period 2001–2012, global warming

experienced a hiatus. This result is similar to that of previous studies and can be attributed to equatorial Pacific surface cooling (Kosaka and Xie, 2013; Li and Zha, 2019). Spatially, the trends of annual mean Ta were generally similar among various datasets. The warming trends were higher in the Arctic region than in the other regions, followed by Eastern Europe and the Middle East (Fig. 11). Insignificant cooling trend was observed in Central Asia. The primary reason for significant warming trend in Arctic region is that an increase in temperature will lead to the melting of snow and ice. The albedo of other land cover types (e.g., open water and vegetation) is generally lower than those of snow and ice. As a result, the Earth's surface absorbs more solar radiation, and further increases the temperature. Note that the trends of mean Ta derived from GSHTD in Antarctica vary greatly in space, which is different from other datasets. The reason for this is not very clear, but may be attributed to: (1) high spatial resolution of GSHTD; and (2) low accuracy of GSHTD in Antarctica (Fig. 6). As meteorological stations are sparsely distributed in Antarctica, it is difficult to accurately estimate Ta and reveal the trends of Ta. Future studies could use more stations to reveal the trends of Ta and improve the accuracy of estimated Ta in Antarctica.

5. Discussion

This study developed a GSHTD, which will be useful in many studies related to climate change (Guo et al., 2019; Li and Zha, 2019; Zhou and Wang, 2016), agriculture and forestry (Blum et al., 2013; Yang et al., 2020), environmental science and ecology (Anniballe et al., 2014; Clinton and Gong, 2013; Yao et al., 2021a), and epidemiology and human health (Weiss et al., 2014b). The GSHTD has four main advantages. First, includes seven types of temperature data: clear-sky daytime and nighttime Ts, all-sky daytime and nighttime Ts, and mean, maximum and minimum Ta. Second, it has global coverage and high spatial resolution (30 arcsecond resolution). Third, using the ETD method proposed in this study, the GSHTD has no missing values. Fourth, the accuracy of the GSHTD is satisfactory. The average MAEs of ETD in filling 25×25 and 150×150 pixel gaps in the daytime (nighttime) Ts data were 0.724 (0.552) $^{\circ}\text{C}$ and 1.024 (0.895) $^{\circ}\text{C}$, respectively. The accuracy of ETD was significantly higher than that of the other two methods. Additionally, although the developed Ta data has global coverage and high spatial resolution, the accuracy of the estimated Ta was higher than that of most previous studies (Benali et al., 2012; Li et al., 2018b; Rao et al., 2019; Shen et al., 2020; Yoo et al., 2018; Zhang et al., 2016). Hooker et al. (2018) developed global monthly mean Ta data with 3 arcmin resolution from 2003 to 2016. The average RMSEs of the estimated monthly mean Ta in this study and

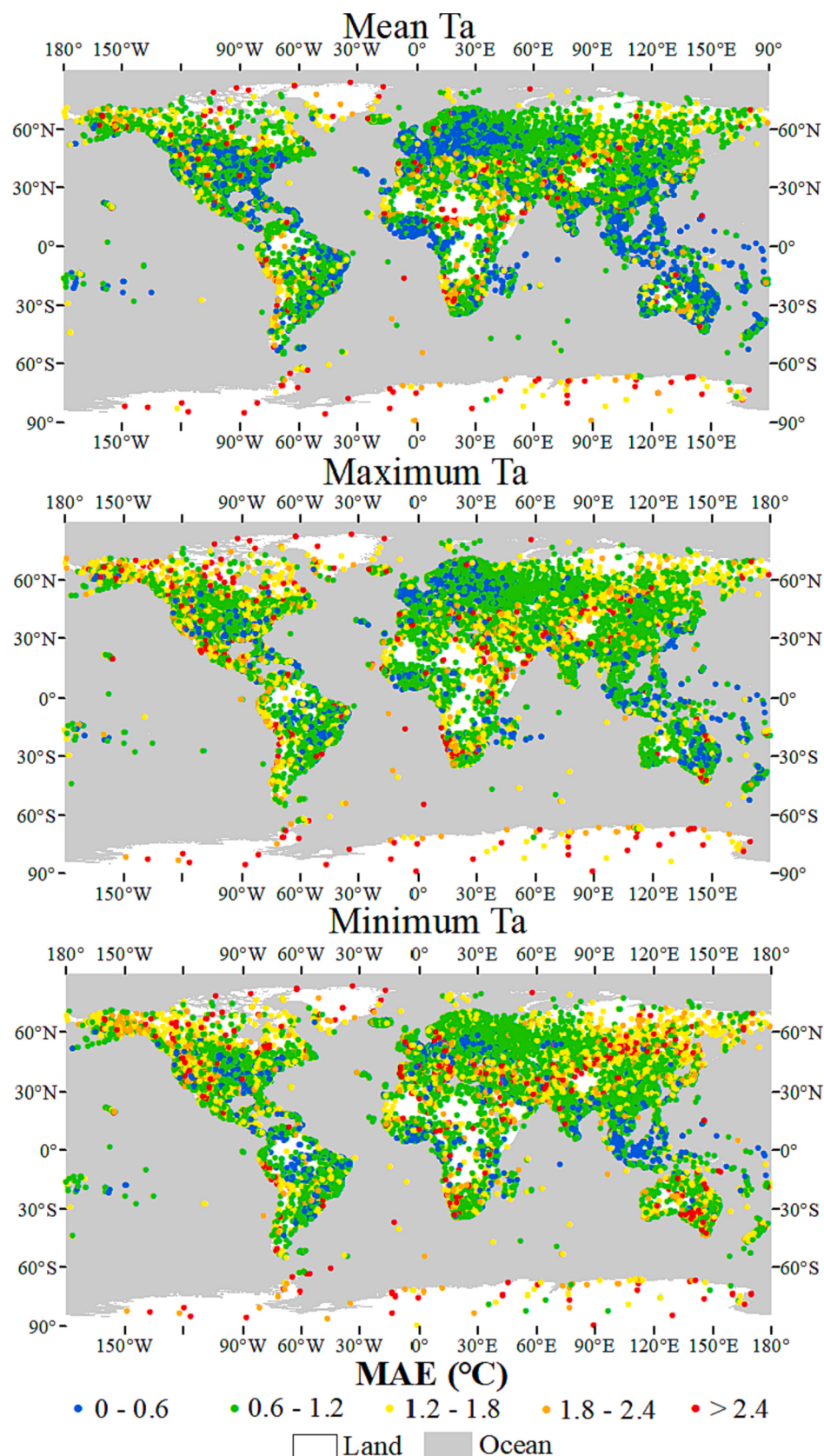


Fig. 6. Spatial distributions of the MAEs of estimated Ta.

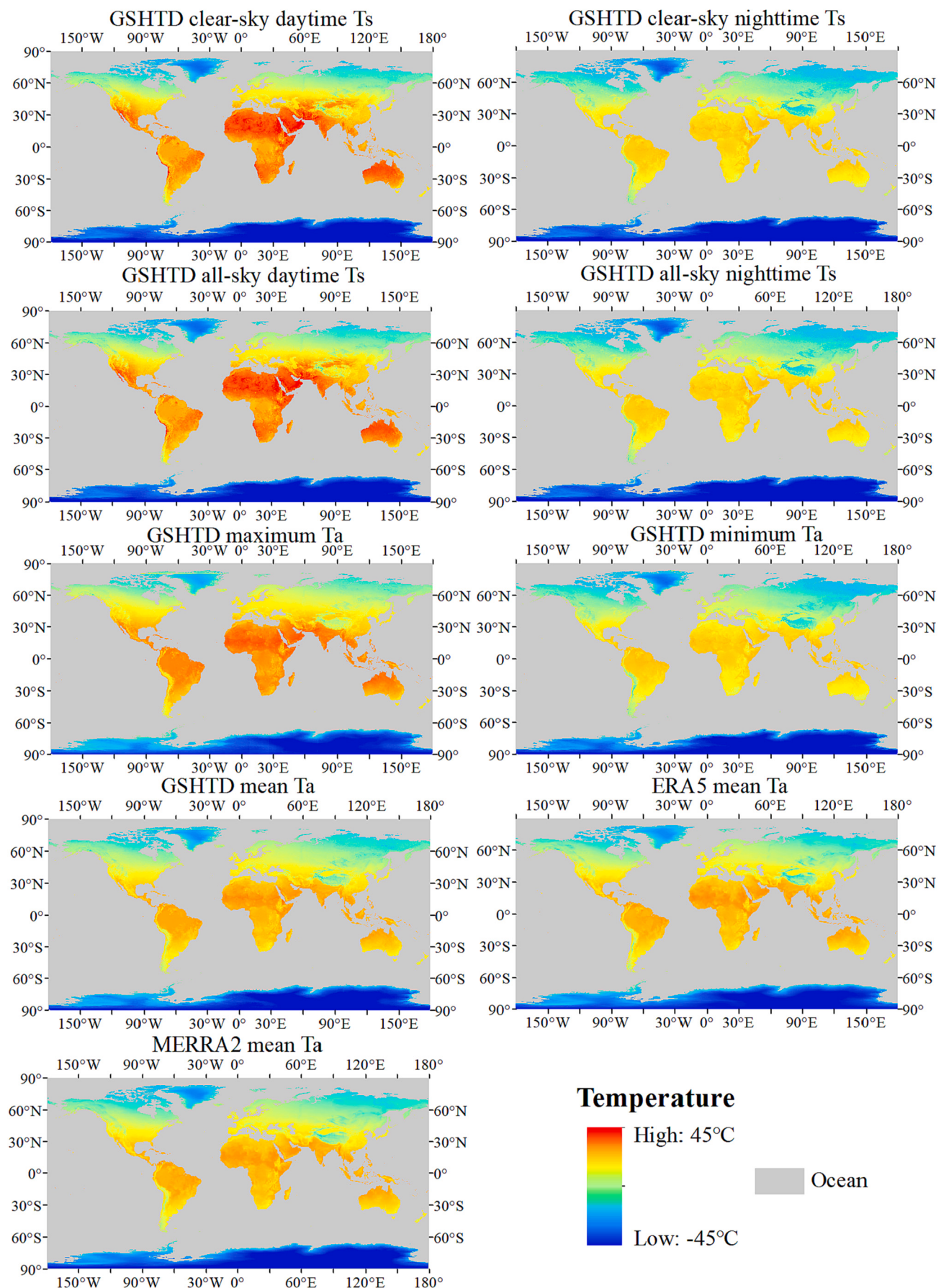


Fig. 7. Spatial variations in Ts and Ta averaged from 2001 to 2020.

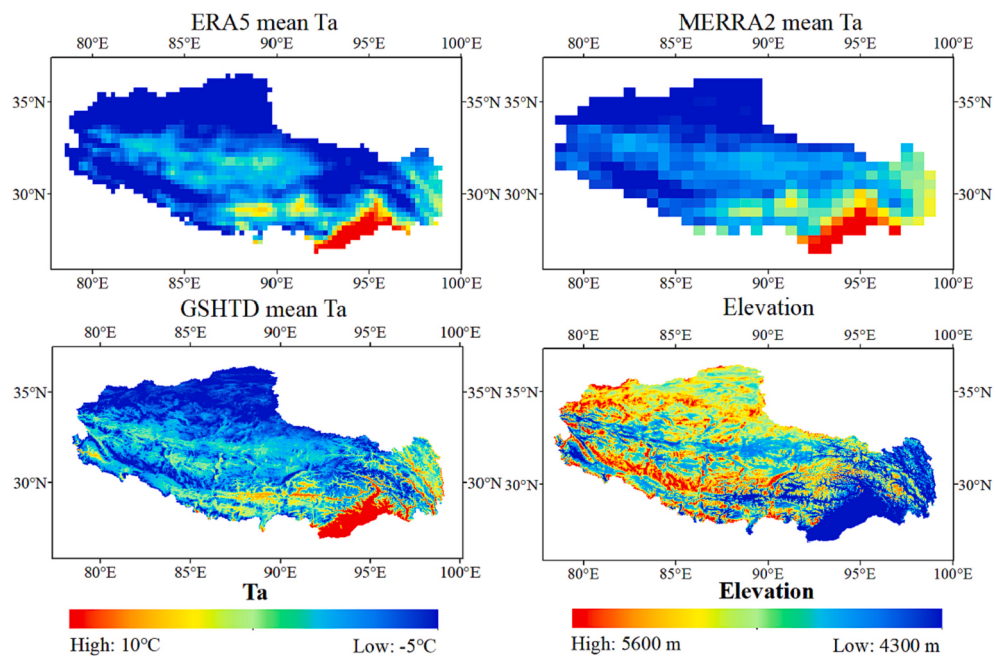


Fig. 8. Spatial variations of Ta in Qinghai-Tibet Plateau averaged from 2001 to 2020.

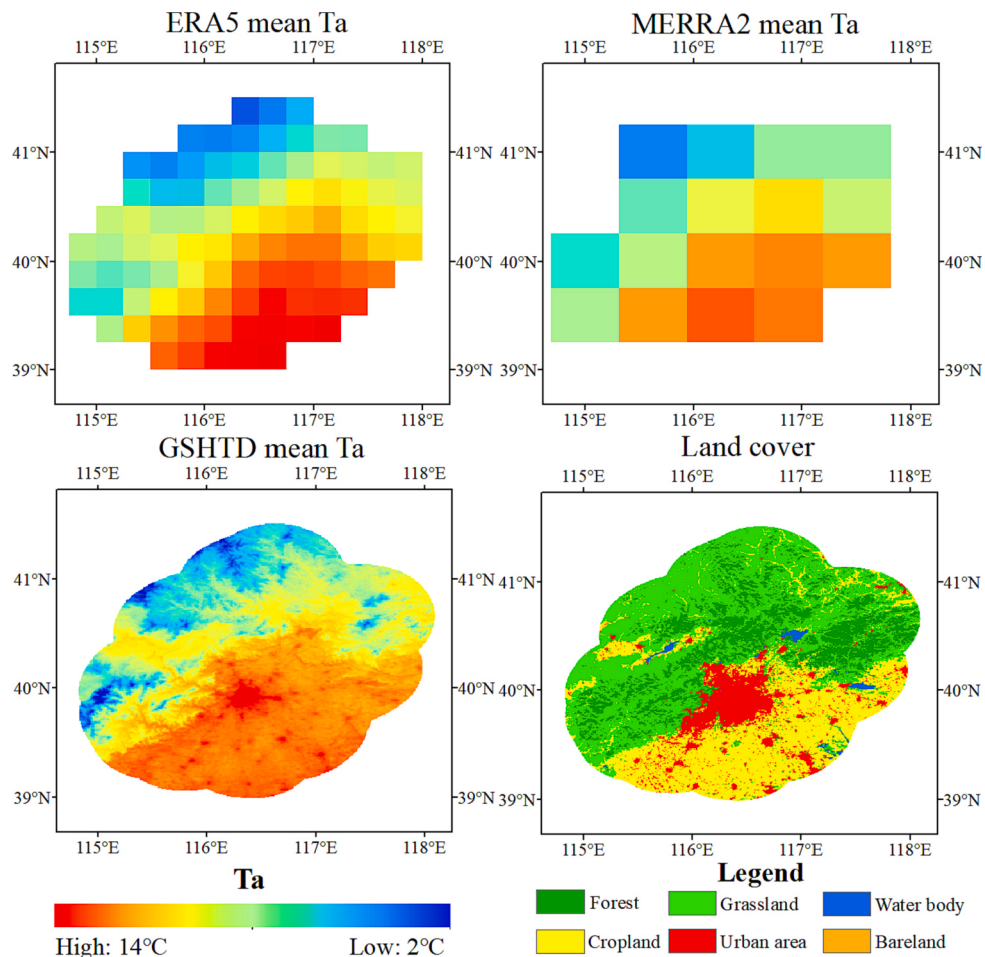


Fig. 9. Spatial distributions of Ts, Ta and land cover types in Beijing (China) and its surrounding area in 2020.

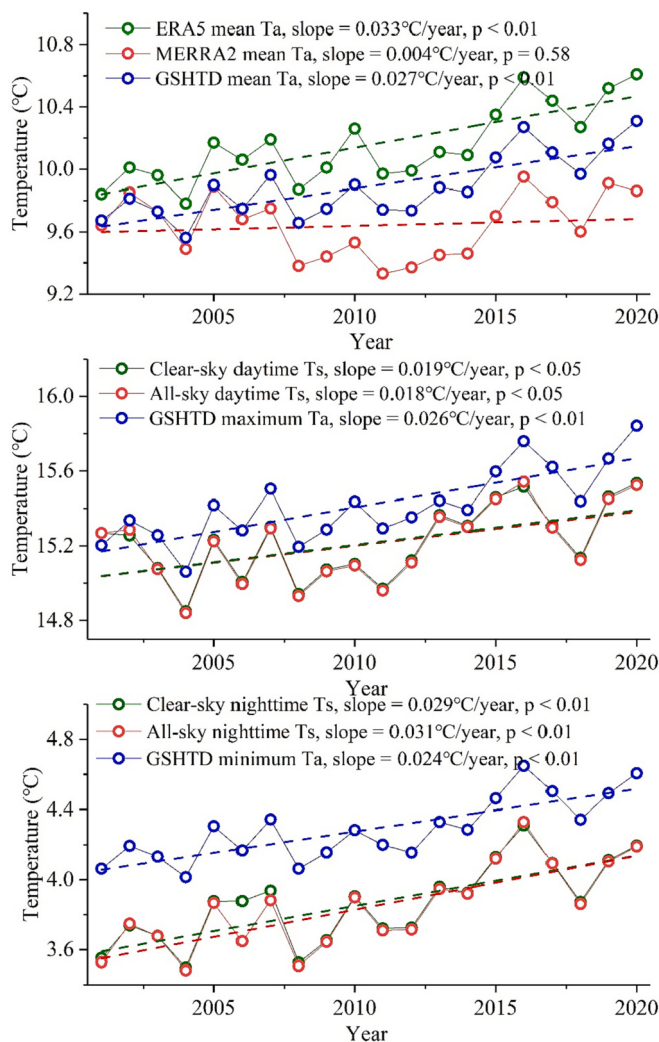


Fig. 10. Trends of annual mean Ts and Ta from 2001 to 2020.

Hooker et al. (2018) were 1.209 and 1.280 °C, respectively. It can be seen that both the spatial resolution and accuracy of the estimated Ta in this study were higher than those in Hooker et al. (2018). The reasons for the high accuracy of the estimated Ta data are as follows. First, this study input the data into the model for different months separately; this strategy can improve the accuracy of the estimated Ta (Yao et al., 2020a). Second, we used 12 predictor variables to estimate the Ta, and only retained 6 predictor variables that have positive impacts on the Ta estimation. Third, the Cubist algorithm has a higher accuracy than other algorithms (Xu et al., 2018; Zhang et al., 2016).

A method called ETD was proposed to fill the gaps in the MODIS Ts data. The main advantage of ETD is its high precision. The MAEs of ETD were, on average, 23.2% lower than that of RSDAST and 23.7% lower than that of IMA. The reason for the high accuracy of ETD is that it avoids the limitations of the other two gapfilling methods (mentioned in Section 4.1.1). Additionally, the computing cost of the ETD method is acceptable and can be used in studies on a global scale. This is because ETD is designed reasonably.

Both estimated gridded Ta and observed point Ta data have their advantages. The gridded Ta data can avoid the limitation that most meteorological stations are located in urban and suburban areas. For example, by using the gridded Ta data, the average warming trend of a region can be calculated as the spatial average warming trend for all pixels. Note that when calculating the regional average warming trend, urban pixels with higher warming trend should be included because

urban area is a part of this region. By using the Ta data of meteorological stations, the regional average warming trend was calculated as follows. First, in each 5×5 grid, the warming trend was calculated as the average warming trend of all stations. Subsequently, the regional average warming trend was calculated as the weighted average warming trend of all 5×5 grids (the area of each grid was used as weight) (Ren and Zhou, 2014; Sun et al., 2016). The latter has uncertainty because: (1) most stations are located in urban and suburban areas; and (2) urban stations are affected by the UHI effect. Although urban areas have little influence on warming at the global scale (Varquez and Kanda, 2018), they have non-negligible influence at the regional and local scales (Chao et al., 2020). Some good practice would reduce uncertainties. For example, excluding stations if they are not fully representative of the area (Varquez and Kanda, 2018), and/or constructing a weighting that links station to the type of land cover within the grid (Wang et al., 2015). However, the accuracy of station-based method may still be lower than that of the method in this study. First, the number of meteorological stations of some land cover types (e.g., natural vegetation) is very small in a region. The station-based method will be affected by the uneven distribution of meteorological stations. Comparatively, this study used samples from the world to estimate Ta. Second, Ta (and its trend) varies by elevation and distance to water body in the same land cover type. The station-based method will be affected by this point but the method used in this study will not. This is because elevation, Ts, latitude and longitude were used to estimate Ta. The observed point Ta data can accurately reflect the climate of a location. Some well sited and representative stations can be adequate to represent the climate of a large homogenous area. In an area with variable land cover, the station could represent different climates with different wind directions as the source area shifts. Furthermore, observed point Ta data can be used to train and validate the estimated Ta at this location.

GSHTD has two main limitations. First, the MODIS Ts data are available from February 2000 to the present. The time series of the GSHTD was only 20 years. Twenty years of data are not sufficient to study climate change. The time series of GSHTD should be extended when a longer time series of MODIS Ts data becomes available in the future. Second, the accuracy of the estimated Ta data was relatively low in polar regions, because the density of meteorological stations is low in these regions. Note that the accuracy evaluation of Ta estimation will also be affected by the sparse distribution of meteorological stations in polar regions. Because the number of stations increases with time (Fig. 1a–1c), future studies could use more stations to estimate and validate Ta in these regions. Furthermore, in situ Ta data from multiple databases can be fused to use, but attention should be paid to the differences (e.g., instrument, observing practices and post-observation processing) between different datasets (Yun et al., 2019).

Some variables that closely correlate with Ta were not used to estimate Ta, such as soil moisture, and wind speed and direction. This is because 30 arcsecond resolution soil moisture and wind data are currently unavailable. Future studies should use these variables to further improve the accuracy of Ta estimation when 30 arcsecond resolution of these data become available.

6. Conclusions

In this study, global seamless Ts and Ta data with 30 arcsecond resolution from 2001 to 2020 were developed. The ETD method was proposed to fill the gaps in the MODIS Ts data. The MAEs of ETD were, on average, 23.2% lower than that of RSDAST and 23.7% lower than that of IMA. Subsequently, a global seamless 8-day and 1-month average Ts dataset (including both all- and clear-sky Ts) was developed using the MODIS Ts data and the ETD method. Finally, a seamless monthly average of the mean, maximum and minimum Ta data was created using the seamless Ts data, in situ Ta data and the Cubist machine learning algorithm. The average MAEs of the estimated monthly average of the mean, maximum and minimum Ta data were 0.797, 0.994 and 1.056 °C,

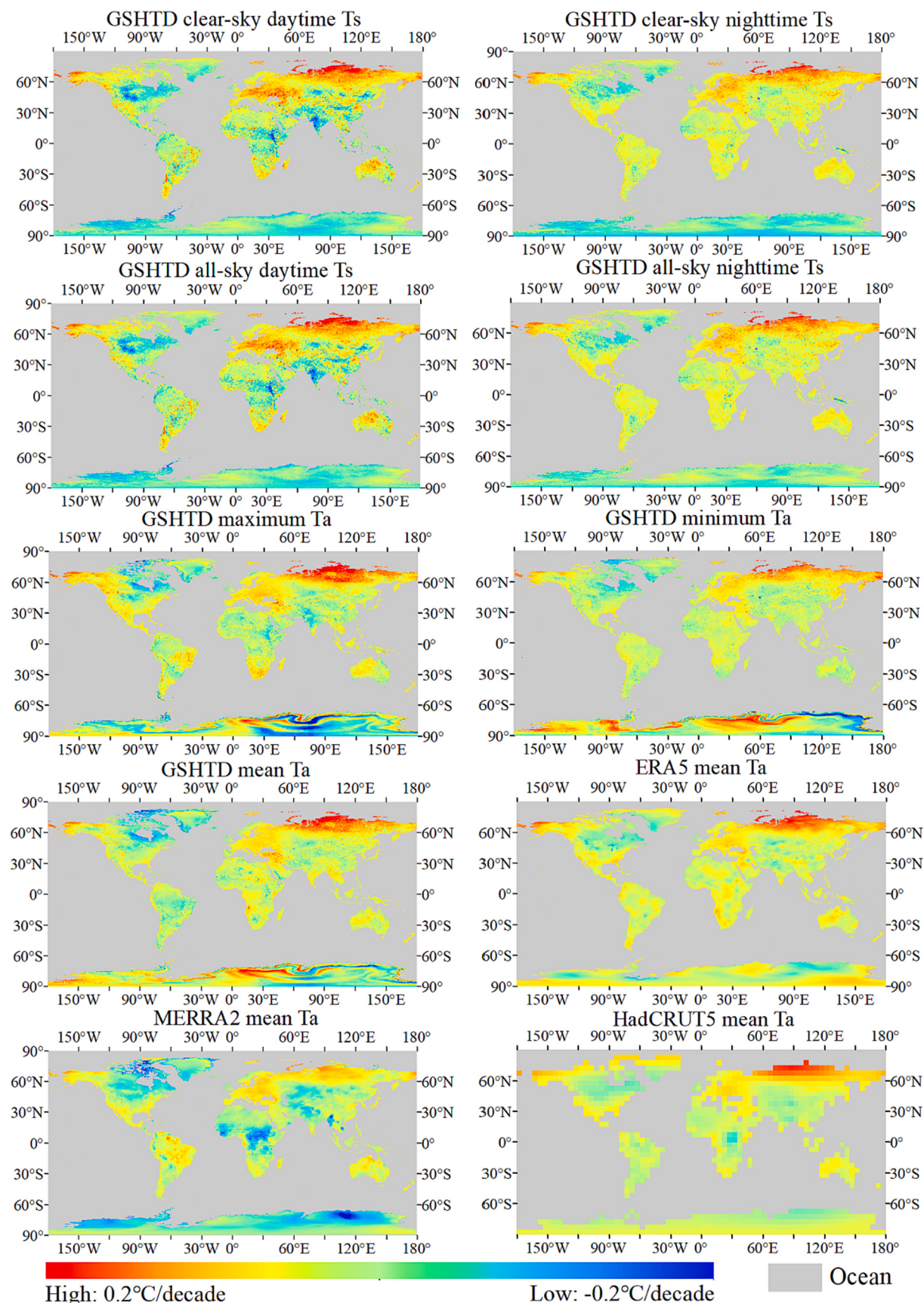


Fig. 11. Spatial distributions of trends of annual mean Ts and Ta from 2001 to 2020.

respectively.

GSHTD has some advantages compared with other datasets: (1) GSHTD has seven types of temperature data; (2) GSHTD has global coverage and high spatial resolution; (3) there are no missing values in GSHTD; and (4) the accuracy of GSHTD is high. The gaps in the Ts data were accurately filled using the ETD method. Additionally, the accuracy of the estimated Ta data was higher than that of most previous studies. Therefore, the GSHTD will be useful in many studies related to climate change, environmental science and ecology, and epidemiology and human health. Future studies should: (1) extend the time series of GSHTD; and (2) improve the accuracy of the estimated Ta data, especially in polar regions.

Credit author statement

Rui Yao: Data curation, Writing- Original draft preparation.

Lunche Wang: Conceptualization, Methodology, Software, Reviewing and Editing, Supervision, Project administration, Funding acquisition.

Xin Huang: Methodology, Software, Supervision.

Qian Cao: Methodology, Software,

Jing Wei: Methodology, Software,

Panxing He: Methodology, Software.

Shaoqiang Wang: Software, Methodology.

Lizhe Wang: Software, Methodology.

Declaration of Competing Interest

The authors declare that they have no known competing financial interests or personal relationships that could have appeared to influence the work reported in this paper.

Data availability

Data will be made available on request.

Acknowledgement

This work was financially supported by the National Natural Science Foundation of China (No.41975044, 41771360, 41801021, 42101385), Open Fund of Hubei Luojia Laboratory (No.2201000043) and the Fundamental Research Funds for National Universities, China University of Geosciences, Wuhan.

Appendix A. Supplementary data

Supplementary data to this article can be found online at <https://doi.org/10.1016/j.rse.2022.113422>.

References

- Anniballe, R., Bonafoni, S., Pichierri, M., 2014. Spatial and temporal trends of the surface and air heat island over Milan using MODIS data. *Remote Sens. Environ.* 150, 163–171.
- Benali, A., Carvalho, A.C., Nunes, J.P., Carvalhais, N., Santos, A., 2012. Estimating air surface temperature in Portugal using MODIS LST data. *Remote Sens. Environ.* 124, 108–121.
- Blum, M., Lensky, I.M., Nestel, D., 2013. Estimation of olive grove canopy temperature from MODIS thermal imagery is more accurate than interpolation from meteorological stations. *Agric. For. Meteorol.* 176, 90–93.
- Bradley, R.S., Keimig, F.T., Diaz, H.F., 1992. Climatology of surface-based inversions in the north american Arctic. *J. Geophys. Res.* 97 (D14), 15699–15712.
- Chadburn, S.E., Burke, E.J., Cox, P.M., Friedlingstein, P., Hugelius, G., Westermann, S., 2017. An observation-based constraint on permafrost loss as a function of global warming. *Nat. Clim. Chang.* 7, 340–344.
- Chao, L., Huang, B., Yang, Y., Jones, P., Cheng, J., Yang, Y., et al., 2020. A new evaluation of the role of urbanization to warming at various spatial scales: evidence from the Guangdong-Hong Kong-Macau region, China. *Geophys. Res. Lett.* 47, e2020GL089152.
- Clinton, N., Gong, P., 2013. MODIS detected surface urban heat islands and sinks: global locations and controls. *Remote Sens. Environ.* 134, 294–304.
- Collins, G.Q., Heaton, M.J., Hu, L., Monaghan, A.J., 2017. Spatiotemporal multiresolution modeling to infill missing areal data and enhance the temporal frequency of infrared satellite images. *Environmetrics* 2017, e2466.
- Coops, N.C., Duro, D.C., Wulder, M.A., Han, T., 2007. Estimating afternoon MODIS land surface temperatures (LST) based on morning MODIS overpass, location and elevation information. *Int. J. Remote Sens.* 28, 2391–2396.
- Crosson, W.L., Al-Hamdan, M.Z., Hemmings, S.N.J., Wade, G.M., 2012. A daily merged MODIS aqua-Terra land surface temperature data set for the conterminous United States. *Remote Sens. Environ.* 119, 315–324.
- Danielson, J.J., Gesch, D.B., 2011. Global multi-resolution terrain elevation data 2010 (GMTED2010). U.S. Geological Survey Open-File Report 2011–1073.
- Duan, S.-B., Li, Z.-L., Leng, P., 2017. A framework for the retrieval of all-weather land surface temperature at a high spatial resolution from polar-orbiting thermal infrared and passive microwave data. *Remote Sens. Environ.* 195, 107–117.
- Fick, S.E., Hijmans, R.J., 2017. WorldClim 2: new 1-km spatial resolution climate surfaces for global land areas. *Int. J. Climatol.* 37, 4302–4315.
- Gao, M., Li, Z., Tan, Z., Li, H., Peng, J., 2021. Use of Google earth engine to generate a 20-year 1 km × 1 km monthly air temperature product over Yellow River Basin. *IEEE J. STARS* 14, 10079–10090.
- Gelaro, R., McCarty, W., Suarez, M.J., Todling, R., Molod, A., Takacs, L., et al., 2017. The modern-era retrospective analysis for research and applications, version 2 (MERRA-2). *J. Clim.* 30, 5419–5454.
- Gerber, F., de Jong, R., Schaepman, M., Schaepman-Strub, G., Furrer, R., 2018. Predicting missing values in spatio-temporal remote sensing data. *IEEE T. Geosci. Remote.* 56, 2841–2853.
- Guo, D., Sun, J., Yang, K., Pepin, N., Xu, Y., 2019. Revisiting recent elevation-dependent warming on the tibetan plateau using satellite-based data sets. *J. Geophys. Res. Atmos.* 124, 8511–8521.
- Hereher, M.E., El Kenawy, A., 2020. Extrapolation of daily air temperatures of Egypt from MODIS LST data. *Geocarto Int.* 1–17.
- Hersbach, H., Bell, B., Berrisford, P., Hirahara, S., Horányi, A., Muñoz-Sabater, J., et al., 2020. The ERA5 global reanalysis. *Q. J. R. Meteorol. Soc.* 146, 1999–2049.
- Hooker, J., Duveiller, G., Cescatti, A., 2018. A global dataset of air temperature derived from satellite remote sensing and weather stations. *Sci. Data* 5, 180246.
- Hu, L., Brunsell, N.A., 2013. The impact of temporal aggregation of land surface temperature data for surface urban heat island (SUHI) monitoring. *Remote Sens. Environ.* 134, 162–174.
- Ke, L., Ding, X., Song, C., 2013. Reconstruction of time-series MODIS LST in Central Qinghai-Tibet plateau using geostatistical approach. *IEEE Geosci. Remote Sens. Lett.* 10 (6), 1602–1606.
- Kosaka, Y., Xie, S.P., 2013. Recent global-warming hiatus tied to equatorial Pacific surface cooling. *Nature* 501, 403–407.
- Leihy, R.I., Duffy, G.A., Nortje, E., Chown, S.L., 2018. High resolution temperature data for ecological research and management on the Southern Ocean islands. *Sci. Data* 5, 180177.
- Li, H., Zhou, Y., Wang, X., Zhou, X., Zhang, H., Sodoudi, S., 2019. Quantifying urban heat island intensity and its physical mechanism using WRF/UCM. *Sci. Total Environ.* 650, 3110–3119.
- Li, L., Zha, Y., 2019. Satellite-based regional warming hiatus in China and its implication. *Sci. Total Environ.* 648, 1394–1402.
- Li, X., Zhou, Y., Asrar, G.R., Zhu, Z., 2018a. Creating a seamless 1 km resolution daily land surface temperature dataset for urban and surrounding areas in the conterminous United States. *Remote Sens. Environ.* 206, 84–97.
- Li, X., Zhou, Y., Asrar, G.R., Zhu, Z., 2018b. Developing a 1 km resolution daily air temperature dataset for urban and surrounding areas in the conterminous United States. *Remote Sens. Environ.* 215, 74–84.
- Li, Y., Wang, X., Chen, Y., Wang, M., 2020. Land surface temperature variations and their relationship to fractional vegetation coverage in subtropical regions: A case study in Fujian Province, China. *Int. J. Remote Sens.* 41, 2081–2097.
- Liu, H., Huang, B., Zhan, Q., Gao, S., Li, R., Fan, Z., 2021. The influence of urban form on surface urban heat island and its planning implications: evidence from 1288 urban clusters in China. *Sustain. Cities Soc.* 71, 102987.
- Liu, X., Zhou, Y., Yue, W., Li, X., Liu, Y., Lu, D., 2020. Spatiotemporal patterns of summer urban heat island in Beijing, China using an improved land surface temperature. *J. Clean. Prod.* 257, 120529.
- Liu, Z., Zhan, W., Lai, J., Hong, F., Quan, J., Bechtel, B., et al., 2019. Balancing prediction accuracy and generalization ability: a hybrid framework for modelling the annual dynamics of satellite-derived land surface temperatures. *ISPRS J. Photogramm.* 151, 189–206.
- Long, D., Yan, L., Bai, L., Zhang, C., Li, X., Lei, H., et al., 2020. Generation of MODIS-like land surface temperatures under all-weather conditions based on a data fusion approach. *Remote Sens. Environ.* 246, 111863.
- Lu, N., Liang, S., Huang, G., Qin, J., Yao, L., Wang, D., et al., 2018. Hierarchical bayesian space-time estimation of monthly maximum and minimum surface air temperature. *Remote Sens. Environ.* 211, 48–58.
- Marthews, T.R., Dadson, S.J., Lehner, B., Abele, S., Gedney, N., 2015. High-resolution global topographic index values for use in large-scale hydrological modelling. *Hydroclim. Earth Syst. Sci.* 19, 91–104.
- Mata, N., Pedreros, D., Dinku, T., Meiburg, A., Budde, M., Rowland, J., et al., 2019. A high-resolution 1983–2016 *tmax* climate data record based on infrared temperatures and stations by the climate Hazard center. *J. Clim.* 32, 5639–5658.
- Metz, M., Andreo, V., Neteler, M., 2017. A new fully gap-free time series of land surface temperature from MODIS LST data. *Remote Sens.* 9, 1333.

- Militino, A.F., Ugarte, M.D., Montesino, M., 2019a. Filling missing data and smoothing altered data in satellite imagery with a spatial functional procedure. *Stoch. Environ. Res. Risk A* 33, 1737–1750.
- Militino, A.F., Ugarte, M.D., Perez-Goya, U., Genton, M.G., 2019b. Interpolation of the mean anomalies for cloud filling in land surface temperature and normalized difference vegetation index. *IEEE T. Geosci. Remote.* 57, 6068–6078.
- Morcel, C.P., Kennedy, J.J., Rayner, N.A., Winn, J.P., Hogan, E., Killick, R.E., Dunn, R.J.H., Osborn, T.J., Jones, P.D., Simpson, I.R., 2021. An updated assessment of near-surface temperature change from 1850: The HadCRUT5 data set. *J. Geophys. Res. Atmos.* 126, e2019JD032361.
- Neteler, M., 2010. Estimating daily land surface temperatures in mountainous environments by reconstructed MODIS LST data. *Remote Sens.* 2, 333–351.
- Noi, P., Degener, J., Kappas, M., 2017. Comparison of multiple linear regression, cubist regression, and random Forest algorithms to estimate daily air surface temperature from dynamic combinations of MODIS LST data. *Remote Sens.* 9 (5), 398.
- Peng, S., Piao, S., Ciais, P., Friedlingstein, P., Ottle, C., Breon, F.M., et al., 2012. Surface urban heat island across 419 global big cities. *Environ. Sci. Technol.* 46, 696–703.
- Pham, H.T., Kim, S., Marshall, L., Johnson, F., 2019. Using 3D robust smoothing to fill land surface temperature gaps at the continental scale. *Int. J. Appl. Earth Obs. Geoinform.* 82, 101879.
- Ramamurthy, P., Bou-Zeid, E., 2017. Heatwaves and urban heat islands: a comparative analysis of multiple cities. *J. Geophys. Res. Atmos.* 122, 168–178.
- Rao, Y., Liang, S., Wang, D., Yu, Y., Song, Z., Zhou, Y., et al., 2019. Estimating daily average surface air temperature using satellite land surface temperature and top-of-atmosphere radiation products over the tibetan plateau. *Remote Sens. Environ.* 234, 111462.
- Ren, G., Zhou, Y., 2014. Urbanization effect on trends of extreme temperature indices of National Stations over mainland China, 1961–2008. *J. Clim.* 27, 2340–2360.
- Ribeiro, I., Martilli, A., Falls, M., Zonato, A., Villalba, G., 2021. Highly resolved WRF-BEP/BEM simulations over Barcelona urban area with LCZ. *Atmos. Res.* 248, 105220.
- Rosenfeld, A., Dorman, M., Schwartz, J., Novack, V., Just, A.C., Kloog, I., 2017. Estimating daily minimum, maximum, and mean near surface air temperature using hybrid satellite models across Israel. *Environ. Res.* 159, 297–312.
- Shen, H., Jiang, Y., Li, T., Cheng, Q., Zeng, C., Zhang, L., 2020. Deep learning-based air temperature mapping by fusing remote sensing, station, simulation and socioeconomic data. *Remote Sens. Environ.* 240, 111692.
- Shwetha, H.R., Kumar, D.N., 2016. Prediction of high spatio-temporal resolution land surface temperature under cloudy conditions using microwave vegetation index and ANN. *ISPRS J. Photogramm.* 117, 40–55.
- Sitzen, S., Sandholt, I., Nørgaard, A., Fensholt, R., Eklundh, L., 2007. Estimation of diurnal air temperature using MSG SEVIRI data in West Africa. *Remote Sens. Environ.* 110, 262–274.
- Sun, L., Chen, Z., Gao, F., Anderson, M., Song, L., Wang, L., et al., 2017. Reconstructing daily clear-sky land surface temperature for cloudy regions from MODIS data. *Comput. Geosci.* 105, 10–20.
- Sun, Y., Zhang, X., Ren, G., Zwiers, F.W., Hu, T., 2016. Contribution of urbanization to warming in China. *Nat. Clim. Chang.* 6, 706–709.
- Varquez, A.C.G., Kanda, M., 2018. Global urban climatology: a meta-analysis of air temperature trends (1960–2009). *NPJ Clim. Atmos. Sci.* 1, 32.
- Wang, F., Ge, Q., Wang, S., Li, Q., Jones, P.D., 2015. A new estimation of Urbanization's contribution to the warming trend in China. *J. Clim.* 28, 8923–8938.
- Wang, K., Liang, S., 2009. Evaluation of ASTER and MODIS land surface temperature and emissivity products. *Remote Sens. Environ.* 113, 1556–1565.
- Wang, M., Yan, X., 2015. A comparison of two methods on the climatic effects of urbanization in the Beijing-Tianjin-Hebei metropolitan area. *Adv. Meteorol.* 2015, 1–12.
- Wang, T., Shi, J., Ma, Y., Husi, L., Comyn-Platt, E., Ji, D., et al., 2019. Recovering land surface temperature under cloudy skies considering the solar-cloud-satellite geometry: application to MODIS and Landsat-8 data. *J. Geophys. Res. Atmos.* 124, 3401–3416.
- Weiss, D.J., Atkinson, P.M., Bhatt, S., Mappin, B., Hay, S.I., Gething, P.W., 2014a. An effective approach for gap-filling continental scale remotely sensed time-series. *ISPRS J. Photogramm.* 98, 106–118.
- Weiss, D.J., Bhatt, S., Mappin, B., Boeckel, T.P.V., Smith, D.L., Hay, S.I., et al., 2014b. Air temperature suitability for plasmodium falciparum malaria transmission in Africa 2000–2012: a high-resolution spatiotemporal prediction. *Malaria J.* 13, 171.
- Xu, Y., Knudby, A., Shen, Y., Liu, Y., 2018. Mapping monthly air temperature in the tibetan plateau from MODIS data based on machine learning methods. *IEEE J. STARS.* 11, 345–354.
- Xu, Y., Shen, Y., 2013. Reconstruction of the land surface temperature time series using harmonic analysis. *Comput. Geosci.* 61, 126–132.
- Yang, S., Zhang, D., Sun, L., Wang, Y., Gao, Y., 2020. Assessing drought conditions in cloudy regions using reconstructed land surface temperature. *J. Meteorol. Res.* 34, 264–279.
- Yao, R., Wang, L., Huang, X., Gong, W., Xia, X., 2019. Greening in rural areas increases the surface urban Heat Island intensity. *Geophys. Res. Lett.* 46, 2204–2212.
- Yao, R., Wang, L., Huang, X., Li, L., Sun, J., Wu, X., et al., 2020a. Developing a temporally accurate air temperature dataset for mainland China. *Sci. Total Environ.* 706, 136037.
- Yao, R., Wang, L., Huang, X., Liu, Y., Niu, Z., Wang, S., et al., 2021a. Long-term trends of surface and canopy layer urban heat island intensity in 272 cities in the mainland of China. *Sci. Total Environ.* 772, 145607.
- Yao, R., Wang, L., Huang, X., Sun, L., Chen, R., Wu, X., et al., 2021b. A robust method for filling the gaps in MODIS and VIIRS land surface temperature data. *IEEE T. Geosci. Remote* 1–15.
- Yao, R., Wang, L., Wang, S., Wang, L., Wei, J., Li, J., 2020. A detailed comparison of MYD11 and MYD21 land surface temperature products in mainland China. *Int. J. Digit. Earth* 1–17.
- Yoo, C., Im, J., Park, S., Quackenbush, L.J., 2018. Estimation of daily maximum and minimum air temperatures in urban landscapes using MODIS time series satellite data. *ISPRS J. Photogramm.* 137, 149–162.
- Yu, P., Zhao, T., Shi, J., Ran, Y., Jia, L., Ji, D., Xue, H., 2022. Global spatiotemporally continuous MODIS land surface temperature dataset. *Sci. Data* 9, 143.
- Yu, W., Tan, J., Ma, M., Li, X., She, X., Song, Z., 2019. An effective similar-pixel reconstruction of the high-frequency cloud-covered areas of Southwest China. *Remote Sens.* 11, 336.
- Yun, X., Huang, B., Cheng, J., Xu, W., Qiao, S., Li, Q., 2019. A new merge of global surface temperature datasets since the start of the 20th century. *Earth Syst. Sci. Data* 11, 1629–1643.
- Zeng, C., Long, D., Shen, H., Wu, P., Cui, Y., Hong, Y., 2018. A two-step framework for reconstructing remotely sensed land surface temperatures contaminated by cloud. *ISPRS J. Photogramm.* 141, 30–45.
- Zeng, C., Shen, H., Zhong, M., Zhang, L., Wu, P., 2015. Reconstructing MODIS LST based on multitemporal classification and robust regression. *IEEE Geosci. Remote S.* 12, 512–516.
- Zeng, Z., Piao, S., Li, L.Z.X., Zhou, L., Ciais, P., Wang, T., et al., 2017. Climate mitigation from vegetation biophysical feedbacks during the past three decades. *Nat. Clim. Chang.* 7, 432–436.
- Zhang, H., Zhang, F., Ye, M., Che, T., Zhang, G., 2016. Estimating daily air temperatures over the tibetan plateau by dynamically integrating MODIS LST data. *J. Geophys. Res. Atmos.* 121, 11425–11441.
- Zhang, M., Wang, B., Cleverly, J., Liu, D., Feng, P., Zhang, H., et al., 2020. Creating new near-surface air temperature datasets to understand elevation-dependent warming in the tibetan plateau. *Remote Sens.* 12, 1722.
- Zhang, Y., Seidel, D.J., Golaz, J.C., Deser, C., Tomas, R.A., 2011. Climatological characteristics of Arctic and Antarctic surface-based inversions. *J. Clim.* 24, 5167–5186.
- Zhang, Y., Song, C., Band, L.E., Sun, G., Li, J., 2017. Reanalysis of global terrestrial vegetation trends from MODIS products: Browning or greening? *Remote Sens. Environ.* 191, 145–155.
- Zhao, B., Mao, K., Cai, Y., Shi, J., Li, Z., Qin, Z., et al., 2020. A combined Terra and Aqua MODIS land surface temperature and meteorological station data product for China from 2003 to 2017. *Earth Syst. Sci. Data* 12, 2555–2577.
- Zhao, W., Duan, S.-B., 2020. Reconstruction of daytime land surface temperatures under cloud-covered conditions using integrated MODIS/Terra land products and MSG geostationary satellite data. *Remote Sens. Environ.* 247, 111931.
- Zhou, C., Wang, K., 2016. Land surface temperature over global deserts: means, variability, and trends. *J. Geophys. Res. Atmos.* 121, 14344–14357.
- Zhou, D., Xiao, J., Frolking, S., Liu, S., Zhang, L., Cui, Y., Zhou, G., 2021. Croplands intensify regional and global warming according to satellite observations. *Remote Sens. Environ.* 264, 112585.
- Zhu, X., Chen, J., Gao, F., Chen, X., Masek, J.G., 2010. An enhanced spatial and temporal adaptive reflectance fusion model for complex heterogeneous regions. *Remote Sens. Environ.* 114, 2610–2623.